Structural Basis for Sarbecovirus Rc-o319 Spike Adaptation to *Rhinolophus cornutus* Bat ACE2 and Constraints on Switching to Human ACE2

Jingjing Wang[1,2,†], Zexuan Li[1,3,†], Yong Ma[1,2,†], Zimu Li[1,4,5], Hang Yuan[1,3], Chuanying Niu[1,6], Banghui Liu[1,2], Mei Li[4], Min Zhou[4], Wenxiu Liu[4], Huimin Feng[1], Jing Chen[4], Jun He[1,2], Xinwen Chen[4,*], Xiaoli Xiong[1,2,*]

1. State Key Laboratory of Respiratory Disease, Guangdong Provincial Key Laboratory of Stem Cell and Regenerative Medicine, Guangdong-Hong Kong Joint Laboratory for Stem Cell and Regenerative Medicine, Guangzhou Institutes of Biomedicine and Health, Chinese Academy of Sciences, Guangzhou 510530, China.

2. Graduate School of Guangzhou Medical University, Guangzhou Medical University-Guangzhou Institutes of Biomedicine and Health Joint School of Life Sciences, Guangzhou Medical University, Guangzhou 511436, China.

3. University of Chinese Academy of Sciences, Beijing 100864, China.

4. Guangzhou National Laboratory, Guangzhou 510005, China.

5. Guangzhou Medical University, Guangzhou 511436, China.

6. University of Science and Technology of China, Hefei 230026, Anhui, China

†These authors contributed equally to this work.

*Corresponding author. Email: chen_xinwen@gzlab.ac.cn (X.C.); xiong_xiaoli@gibh.ac.cn (X.X.)

Abstract

Bat sarbecoviruses often exhibit species-dependent ACE2 specificity. Understanding the determinants of receptor specificity enables better assessment of the cross-species transmission potential of sarbecoviruses. Here, we characterize the S-protein of Rc-o319, a sarbecovirus identified in Japanese *Rhinolophus cornutus* bats. Featuring an unusual 9-amino-acid deletion within its receptor binding motif (RBM), Rc-o319 S-protein utilizes its cognate *R. cornutus* ACE2 ($bACE2_{R.cor}$) but not human ACE2 (hACE2), demonstrating highly restricted receptor specificity. Cryo-EM structures reveal two locked prefusion conformations of the Rc-o319 S-trimer and define a novel Type-4 receptor-binding domain (RBD), featuring a distinct beta-loop (BL) within the RBM due to the RBM-deletion. The Rc-o319-RBD:$bACE2_{R.cor}$ complex structure reveals unique interactions mediated by the specialized BL and RBM-loop of Rc-o319-RBD and by a $bACE2_{R.cor}$ glycan. Structure-guided mutagenesis demonstrates that changes in BL and RBM-loop within the Rc-o319 S-RBD must occur simultaneously to allow medium-to-high-affinity hACE2 binding. Comparative assays further show that the $bACE2_{R.cor}$ receptor supports only a subset of sarbecoviruses, highlighting its restricted sarbecovirus compatibility. Our findings establish the Rc-o319 S-protein as a structurally and functionally specialized adaptation to *R. cornutus* ACE2 and identify the structural constraints limiting its cross-species transmission potential.

Introduction

The SARS-CoV-1 (also known as SARS-CoV) outbreak(1-4) and the SARS-CoV-2 pandemic have profoundly impacted global public health. Surveillance efforts have since detected multiple SARS-related coronaviruses (SARSr-CoVs) primarily in horseshoe bats (genus *Rhinolophus*) worldwide (5-9), suggesting they are the likely natural reservoir for SARSr-CoVs (10-12). Along with SARS-CoV-1 and SARS-CoV-2, SARSr-CoVs have been classified into the *Sarbecovirus* subgenus in the *Betacoronavirus* family (https://ictv.global/taxonomy). Sarbecoviruses share considerable similarity in their spike (S) proteins with amino-acid (AA) sequence identity > 63% (13-18). Like other coronaviruses (CoVs), sarbecovirus S-protein assembles into a large, glycosylated homo-trimer on the virion surface. Each S-protein protomer can be divided into two parts: the S1 part, responsible for cell attachment, and the S2 part, facilitating virus-cell membrane fusion (19-21). For a sarbecovirus S-protein, its S1 parts can be further divided as the N-terminal domain (NTD), receptor binding domain (RBD), Domain C (also called subdomain-1, SD-1) and Domain D (also called subdomain-2, SD-2) (17, 19, 22-25). The S-RBD can be further divided into a core domain, onto which a receptor binding motif (RBM) region is attached (17, 26). The RBM primarily contacts the receptor, forming the interaction interface with the receptor (24, 26-28).

For both SARS-CoV-1 (26, 29) and SARS-CoV-2 (30, 31) their S-RBDs bind with the human ACE2 (hACE) receptor with high affinities in the nano-molar range, suggesting that high-affinity hACE2 binding is likely a key prerequisite for spill-over into the human population. Of note, not all bat SARSr-CoVs can bind hACE2 with high-affinity (5, 7, 12-16, 32, 33). We previously reported that sarbecovirus S-protein can be classified into three types based on their RBM structural features. Four featured RBM regions have been defined, namely the large-loop (LL), lamella (LM), small-loop (SL), and finally the anchor-loop (AL) (17). Type-1 S-proteins, including SARS-CoV-1, SARS-CoV-2 and WIV1, possess intact LL and SL regions. Type-1 S-proteins often bind hACE2, albeit with varying affinities: SARS-CoV-1 and SARS-CoV-2 bind hACE2 with high affinities, whereas WIV1 binds hACE2 with a moderate affinity. We found high-affinity hACE2 binding

requires synergistic favourable hACE2 interactions across the four featured RBM regions. Type-2 S-proteins, including BM48-31 and BtKY72, have an intact LL but a deleted SL. They generally lack hACE binding but can bind selected bat ACE2 (bACE2) orthologs with intermediate affinities. Type-3 S-proteins, including HeB2013 and RmYN02, have both their LL and SL regions deleted. They have yet been reported to bind neither hACE2 nor bACE2.

Ongoing surveillance in Japan has recently discovered several new SARSr-CoVs in the little Japanese horseshoe bat - *Rhinolophus cornutus* (*R.cor*) detected in 2020 using samples collected in 2013 (7). The presentative virus, Rc-o319, is distantly related to SARS-CoV-2, sharing 81% whole-genome identity. Interestingly, although its S-protein has 81% AA identity to SARS-CoV-2 S-protein, its RBM contains a unique nine-amino-acid deletion relative to SARS-CoV-2 that removes residues identified critical for ACE2 binding in other SARSr-CoVs and likely alters its RBM structure (7). Deletions in the RBMs of SARSr-CoVs have been shown to greatly affect ACE2 binding (28, 34). In this study, we surveyed binding of Rc-o319 S-protein to various ACE2 orthologs to understand its specificity. Further, we determined the structures of the Rc-o319 S-trimers and of the Rc-o319-RBD bound to *R. cornutus* ACE2 ($bACE2_{R.cor}$), thereby establishing the Rc-o319 RBD as a novel Type-4 RBD. By analysing the molecular determinants of receptor specificity revealed by our structures, we identify the changes necessary to switch the specificity of the Rc-o319 S-protein to hACE2. These findings provide insights into Rc-o319's adaptations to various ACE2 orthologs and provide an assessment of its cross-species transmission potential.

104 **Results**

105

106 **Rc-o319 S utilizes a narrow range of *Rhinolophus* bat ACE2 orthologs as**
107 **receptors**

108 We used a S:ACE2 interaction mediated cell-cell fusion assay to identify ACE2
109 orthologs that can interact with Rc-o319-S-protein (35). Effector cells expressing
110 Rc-o319 S-proteins were tested against receptor cells expressing a panel of ACE2
111 orthologs for fusion activity (**Fig. 1A**). In this assay, several *Rhinolophus affinis*
112 (*Ra*) and *Rhinolophus sinicus* (*Rs*) ACE2 molecules, including *Ra*5538, *Ra*9479,
113 *Rs*1446, *Rs*3359, and *Rs*3366, were found to mediate varying levels of cell-cell
114 fusion, with *Ra*9479 showing the highest activity and *Rs*3366 the lowest. However,
115 all were substantially weaker than the cognate bACE2$_{R.cor}$ receptor. Rc-o319 S-
116 protein is unable to utilize pangolin and human ACE2 (hACE2) orthologs for
117 fusion. Receptor binding assays using biolayer interferometry (BLI) show that Rc-
118 o319-RBD-Fc and Rc-o319-S-trimer bind bACE2$_{R.cor}$ with moderate-to-high
119 affinities (**Fig.1B** left panels, 76 nM for RBD-Fc and 27 nM for S-trimer**)**.
120 Although Rc-o319 appears to somewhat use bACE2$_{Ra9479}$, showing weak fusion
121 activity in the cell-cell fusion assay. BLI assays were unable to detect bACE2$_{Ra9479}$
122 binding by the Rc-o319 S-trimer and dimeric Rc-o319-RBD-Fc **(Fig.1B**, middle
123 panels**)**. Rc-o319-S-trimer binds bACE2$_{R.cor}$ with relative weak responses and an
124 estimated affinity of 27 nM, tighter than that observed for the dimeric Rc-o319-
125 RBD-Fc, indicating avidity-amplified receptor binding (**Fig.1B,** left panels).
126 Consistent with the cell-cell fusion assay results, neither Rc-o319-RBD-Fc nor Rc-
127 o319-S-trimer is able to bind hACE2 (**Fig.1B**, right panels**)**. These results
128 demonstrate that Rc-o319-S-protein has a restricted ACE2 specificity, with a clear
129 preference towards its cognate bACE2$_{R.cor}$ receptor (**Fig.1A** and **B)**.

130 **Structures of the Rc-o319 S-protein identify a new type of RBM**

131 To understand the unusual restricted receptor specificity of Rc-o319 S-protein,
132 purified Rc-o319 S-protein ectodomain was imaged by cryo-electron microscopy
133 (Cryo-EM) (**Fig. S1**), revealing that Rc-o319 S-trimers adopt two distinct
134 conformations (**Fig. 1D-I, Fig. S1, Fig. S2** and **Fig. S3A**). In both conformations,
135 the 3 RBDs in each S-trimer are all in "down" positions (**Fig. 1D** and **G**). Detailed

136 structural analysis reveals tight trimer packing for both conformations and based
137 on their structural features, the two conformations have been identified as "locked-
138 1" and "locked-2" conformations previously identified for both SARS-CoV-1 and
139 SARS-CoV-2 S-trimers (22, 25, 36-38) (**Fig. 2A** and **B** and **Fig. S2**).

140

141 In the locked-1 Rc-o319 S-trimer, each RBD contains a density that can be
142 modelled as a fatty acid with 18-carbon atoms, previous mass-spectrometry
143 analysis identified it being either linoleic acid (39, 40) or oleic acid (41) (**Fig. 1E**
144 and **Fig. S3C**). Consistent with previous observations, the aliphatic tail of the fatty
145 acid is bound within the hydrophobic fatty-acid binding pocket of one RBD, while
146 its carboxylate group forms salt-bridges with $R382_{Rc\text{-}o319}$ of a neighbouring RBD
147 (**Fig. 1E** and **Fig. S3C**); these fatty acid mediated inter-protomer interactions likely
148 stabilise the S-trimer in the observed locked conformation. Each NTD also
149 contains a density corresponding to a biliverdin molecule. Binding of biliverdin
150 has been correlated with evasion of antibody immunity (42, 43) (**Fig. 1D** and **1G**
151 and **Fig. S3D**). Consistent with being in a locked conformation, the fusion peptide
152 proximal region (FPPR) is ordered (**Fig. 1F**). Finally, consistent with the locked-1
153 conformation observed for the S-proteins of SARS-CoV-1 (25) and SARS-CoV-2
154 (38), residues $580\text{-}605_{Rc\text{-}o319}$ form a large disordered loop within Domain D of the
155 Rc-o319 S-trimer (**Fig. 1D** and **F**).

156

157 In the locked-2 conformation, no fatty acid density was observed within the RBD
158 fatty-acid binding pocket (**Fig. 1H**). This is accompanied with a restructuring of
159 the fatty-acid binding pocket (**Fig. 1H** and **Fig. S3C**) as observed when the fatty-
160 acid binding pockets were vacated in other sarbecovirus S-trimers (39, 44). Each
161 NTD still contains a density corresponds to a biliverdin (**Fig. 1D** and **1G**). The
162 FPPR is ordered (**Fig. 1I**). Differently, the disordered Domain D loop in the
163 locked-1 conformation refolds and forms a large ordered loop structure, packing
164 against the core of the Domain D and the junction between Domains C and D (**Fig.
165 1F**) (25, 38).

166

167 A structural change between locked-1 and locked-2 conformations in the Domain
168 C-D junction region can be observed similar to previous observations on the S-
169 proteins of SARS-CoV-1 and SARS-CoV-2 (25, 38) (**Fig. S3A**). Near the 3-fold
170 axis, to the top of the S-trimer, D468$_{Rc\text{-}o319}$ forms an intra-protomer hydrogen bond
171 with Y473$_{Rc\text{-}o319}$ in the locked-1 conformation (**Fig. 2A**). Whereas in locked-2
172 conformation, D468$_{Rc\text{-}o319}$ mediates two inter-protomer hydrogen bonds with
173 S469$_{Rc\text{-}o319}$ of a neighbouring S-protomer (**Fig. 2B**). Of Note, in both
174 conformations, K458$_{Rc\text{-}o319}$, equivalent to Q493$_{SARS2}$, previously identified as an
175 important determinant for ACE2 specificity (17, 45, 46), is found to form an inter-
176 protomer hydrogen bond to the glycan attaching to N344$_{Rc\text{-}o319}$ of a neighbouring
177 S-protomer (**Fig. 2A-B**). Inter-protomer hydrogen bonds likely contribute to S-
178 trimer stability.

179

180 In both Rc-o319 S-trimer conformations, their NTDs are well resolved, revealing
181 five loops that are markedly shorter than those in SARS-CoV-2 (**Fig. 2C-D** and
182 **Fig. S3E**). In addition, a four-amino-acid insertion (residues 189-192$_{Rc\text{-}o319}$) is
183 identified in the Rc-o319 NTD, forming an "inserted loop" exposed to the exterior
184 of the trimer (**Fig. S3B**). Because the NTD is under strong immune pressure (47,
185 48), these truncated and elongated loops likely endow the NTD of Rc-o319 S-
186 protein with a distinct antigenic profile.

187

188 Finally, Rc-o319 S-trimer structures show that their RBDs form structures distinct
189 from previous characterized sarbecovirus RBDs (**Fig. 2E-G** and **Fig. S4**). In
190 contrast to Type-3 RBDs, where 13- to 14-amino-acid deletions relative to SARS-
191 CoV-2 eliminate the large-loop (LL) (**Fig. S4C** and **S4F-G**), the Rc-o319 RBD
192 retains an extension in a similar region as the LL of Type-1 RBDs, despite a nine-
193 amino-acid deletion (**Fig. 2E**). In the Type-1 RBD, the LL is formed by two half-
194 loops stabilized by an intra-loop disulfide bond (**Fig. 2F**). By contrast, the
195 equivalent extension in the Rc-o319 RBD comprises two small antiparallel β-
196 sheets connected by a short loop (**Fig. 2E** and **Fig. 3**). We designate this distinct
197 extension a beta-loop (BL) structure. Due to the nine-amino-acid deletion, the
198 stabilizing disulfide bond found in the LL is lost.The shorter BL occupies a
199 position roughly corresponding to the C-terminal half-loop of the LL in Type-1

200 RBDs (**Fig. 2E-G** and **Fig. 3D)**, albeit with notable conformational and tilting
201 angle differences (**Fig. 2G,** also see **Fig. 3D**). This distinct beta-loop (BL)
202 structure, by comparison with the LL structure in Type-1 RBDs (**Fig. 2F**), suggests
203 that the Rc-o319-RBD likely binds ACE2 with distinct interactions.

204

205 **Structure of the Rc-o319-RBD:bACE2$_{R.cor}$ complex**

206 To further understand receptor binding by the Rc-o319 S-protein, we determined a
207 structure of Rc-o319-RBD in complex with its cognate bACE2$_{R.cor}$ receptor (**Fig. 3**
208 and **Fig. S1B**). This structure uncovers several previously unrecognized
209 interactions at the Rc-o319-RBD:bACE2$_{R.cor}$ interface, even though the molecular
210 surfaces employed for binding largely mirror those in other sarbecovirus
211 RBD:ACE2 complexes (**Fig. 3A-B**). These interactions are mediated by the
212 specialized RBD BL and RBM-loop and a glycan linked to Asn38 of bACE2$_{R.cor}$
213 (**Fig. 3A, E** and **H-I**) (interfacial residues in the RBD and ACE2 are denoted using
214 single-letter and three-letter amino acid codes, respectively). The buried surface
215 area (BSA) of the complex was calculated as 1005 Å^2, which includes a
216 contribution of 252 Å^2 from the binding of the Asn38-linked glycan. In line with
217 previous interface analysis, the binding interface can be divided into four regions,
218 namely the beta-loop (BL), lamella (LM), anchor loop (AL) and small loop (SL)
219 regions (**Fig. 3F-I)**.

220

221 The beta-loop (BL) of Rc-o319 RBD engages highly distinctive interactions (**Fig.**
222 **3A** and **F**). Due to its distinct structure and protrusion from the RBM, the BL
223 contacts the bACE2$_{R.cor}$ near Lys27, forming a hydrogen bond with the side chain
224 of Lys27 (**Fig. 3A** and **F**). In contrast, LL in Type-1 RBDs contacts ACE2 near
225 residue 24, more towards the ACE2 N-terminus (**Fig. 3J**). Distinctively, BL
226 residue Y447$_{\text{Rc-o319}}$ forms a charged hydrogen bond with Asp31 of bACE2$_{R.cor}$ (**Fig.**
227 **3A** and **F**). Of note, the positively charged residue K454$_{\text{Rc-o319}}$, unique to the Rc-
228 o319 RBM, extends from the BL to form a salt-bridge with Glu75$_{\text{Rc-o319}}$ of
229 bACE2$_{R.cor}$ (**Fig. 3A**) and is positioned in close proximity to the negatively charged
230 bACE2$_{R.cor}$ residues Asp31 and Glu35 (**Fig. 3F-G**). Changing this residue

231 (K454Y$_{Rc\text{-}o319}$) to the corresponding residue Y in SARS-CoV-2 substantially
232 reduced bACE2$_{R.cor}$ binding **(Fig. S8B)**.

233

234 Distinct from SARS-CoV-2, the large Rc-o319 RBM-loop (**Fig. 2E, 3C, 3F** and
235 **Fig. S6**) adjacent and N-terminal to the BL contributes to bACE2$_{R.cor}$ binding and
236 contacts the BL structure with specialized interactions (compare **Fig. 3F** and **Fig.**
237 **3J**): W430$_{Rc\text{-}o319}$ in the RBM-loop forms a cation-π interaction with Lys27 of
238 bACE2$_{R.cor}$, and likely stabilizes the BL via a π-π interaction with the BL residue
239 Y447$_{Rc\text{-}o319}$ (**Fig. 3F**).

240

241 In the lamella (LM) region, K458$_{Rc\text{-}o319}$ forms a salt-bridge with bACE2$_{R.cor}$ Glu35
242 (**Fig. 3G**). Distinctively, in this region, the Asn38-glycan is part of the ACE2-RBD
243 interface, forming hydrogen bonds with N459$_{Rc\text{-}o319}$ (**Fig. 3G**). Also in this region,
244 Lys353$_{Rc\text{-}o319}$ forms a hydrogen bond with the G461$_{Rc\text{-}o319}$ backbone (**Fig. 3G**). In
245 the anchor-loop (AL) region, a hydrogen bond network is observed among
246 bACE2$_{R.cor}$ residues Tyr41, Asn330, Asp335, Arg357 and the RBD residue S465
247 (**Fig. 3H**). Further, the glycan attached to Asn38 of bACE2$_{R.cor}$ forms an inter-
248 molecular hydrogen bond with bACE2$_{R.cor}$ residue Glu42 and also hydrogen bonds
249 with RBD residue Y463$_{Rc\text{-}o319}$ (**Fig. 3H**). Finally, in the small-loop (SL) region,
250 F423$_{Rc\text{-}o319}$ forms a sugar-π contact with the glycan attached to Asn38 (**Fig. 3I**).

251

252 These interactions, by comparison with those used by SARS-CoV-2 to engage
253 ACE2 (**Fig. 3J-M**), show that Rc-o319 RBD engages its cognate bACE2$_{R.cor}$
254 receptor with unique characteristics.

255

256 **Molecular determinates underlying Rc-o319 specificity for bACE2$_{R.cor}$**

257 To understand the specificity of the Rc-o319 S-protein towards the bACE2$_{R.cor}$
258 receptor. We employed a systematic mutagenesis approach to change RBM regions
259 to match those of SARS-CoV-2 (SL mutation = F423Y$_{Rc\text{-}o319}$; LM mutation =
260 K458Q$_{Rc\text{-}o319}$; AL mutation = S465T$_{Rc\text{-}o319}$+A466N$_{Rc\text{-}o319}$+H470Y$_{Rc\text{-}o319}$). This

261 approach has been previously used to elucidate how high-affinity hACE2 binding
262 may be acquired by Type-2 sarbecovirus S-proteins (17). We found that changing
263 AL and SL regions individually had very little effect in improving hACE2 binding
264 (**Fig. 4D** and **E, the second panels**). The SL change retained very strong
265 bACE2$_{R.cor}$ utilization (**Fig. 4E, the third** and **fifth panels**), whereas the AL
266 change substantially reduced bACE2$_{R.cor}$ utilization (**Fig. 4D, the third** and **fifth**
267 **panels**). Changing the LM region reduced bACE2$_{R.cor}$ utilization (**Fig. 4C, the**
268 **first, third** and **fifth panels)** but failed to confer hACE2 mediated fusion activity
269 (**Fig. 4C, the fourth** and **fifth panels**). Swapping of the Rc-o319 BL region to the
270 LL sequence of SARS-CoV-2-RBD, appears to confer Rc-o319 with the ability to
271 utilize hACE2 for cell fusion activity at the expense of substantially reduced fusion
272 activity mediated by its cognate bACE2$_{R.cor}$ receptor (**Fig. 4B**). BLI assay results
273 show that replacing BL with the LL sequence of SARS-CoV-2 greatly reduced
274 bACE2$_{R.cor}$ receptor binding (**Fig. 4B, the first panel**). However, despite
275 conferring cell fusion activity, hACE2 binding by the dimeric BL variant of Rc-
276 o319-RBD-Fc protein was still too weak to be detected **(Fig. 4B, the second panel**
277 and **Fig. S7B)**. These findings are consistent with our previous observations that
278 high-affinity hACE2 binding requires the sarbecovirus RBD to establish optimal
279 contacts across all four RBM regions, with intact LL and SL (17). Similar synergy
280 across multiple RBM regions, conferring high-affinity receptor binding, has also
281 been observed in merbecoviruses (49).

282

283 However, unexpectedly, when we tested the BL+LM+AL+SL variant, enhanced
284 hACE utilization was observed in the cell-cell fusion assay but hACE2 binding
285 was still too weak to be measured in the BLI assay (**Fig. 4F, the second** and
286 **fourth panels**). The BL+LM+AL+SL variant of Rc-o319-RBD-Fc protein also
287 showed no bACE2$_{R.cor}$ binding in BLI assays, and consequently exhibited very
288 little bACE2$_{R.cor}$ mediated fusion activity (**Fig. 4F, the first** and **third panels)**.
289 Therefore, in the case of Rc-o319 S-protein, determinants outside of the BL, LM,
290 AL, and SL regions likely hinder high-affinity hACE binding.

291

292 Structural comparison shows that W430$_{Rc\text{-}o319}$ and S432$_{Rc\text{-}o319}$ in the large RBM-
293 loop (amino acid (AA) 429-442$_{Rc\text{-}o319}$, corresponding to AA 455-468$_{SARS2}$), located

294 N-terminal to the BL, are unique to the Rc-o319 RBD (**Fig. 3C** and **F**, **Fig. S4G**
295 and **S6**). In SARS-CoV-2-RBD, the corresponding residues $F456_{SARS2}$ and
296 $K458_{SARS2}$, respectively interact with the LL residues $Y473_{SARS2}$ and $E471_{SARS2}$
297 (**Fig. 3J** and **Fig. S6A** and **D**). These interactions likely stabilize the SARS-CoV-2
298 LL structure. We introduced these residues into the Rc-o319 BL+SL+LM+AL
299 variant as $W430F_{Rc\text{-}o319}$ and $S432K_{Rc\text{-}o319}$ substitutions (collectively named as the
300 "RBM-loop" mutation), the BLI binding results show that the dimeric
301 BL+SL+LM+AL+RBM-loop variant of Rc-o319-RBD-Fc is able to bind hACE2
302 with a much increased affinity of 31.7 nM (**Fig. 4G**, **the second panel**). We also
303 attempted the swap of Rc-o319 RBM for the SARS-CoV-2 RBM (Rc-o319-RBD-
304 RBM_{SARS2}), as expected, the Rc-o319-RBD-Fc variant with the swapped RBM also
305 showed high-affinity binding to hACE2 with only slightly higher affinity (12.3
306 nM) than the BL+LM+AL+SL +RBM-loop variant (**compare Fig. 4G** and **H**, **the**
307 **second panels**). Consistently, both BL+LM+AL+SL+RBM-loop and RBM
308 swapped Rc-o319-RBD-RBM_{SARS2} show effective hACE2 mediated cell-fusion
309 activities (**Fig. 4G** and **H**, **the fourth** and **fifth panels**).Therefore, our mutagenesis
310 results identify residues in the RBM-loop of Rc-o319 N-terminal to BL contain
311 residues non-compatible with the LL structure of the Type-1 RBD, thereby
312 preventing the LL structure from mediating optimal ACE2 interaction (**Fig. S6C**
313 and **Fig. S7C** and **D**).

314

315 **Utilization of bACE2$_{R.cor}$ by different types of sarbecoviruses**

316 Our structural and biochemical analyses show that the Rc-o319 S-protein has a
317 highly restrictive specificity towards its cognate bACE2$_{R.cor}$ receptor, we further
318 characterize the potential of bACE2$_{R.cor}$ to support diverse sarbecoviruses **(Fig. 4)**.
319 A panel of sarbecovirus S-proteins was surface-expressed on effector cells and
320 tested for cell-cell fusion activity against receptor cells expressing bACE2$_{R.cor}$ (**Fig.**
321 **4I**). The panel included Type-1 RBD S-proteins from SARS-CoV-1, LYRa11,
322 SHC014, WIV1, RaTG13, BANAL-20-52, BANAL-20-236, and the SARS-CoV-2
323 ancestral strain; Type-2 RBD S-proteins from BtKY72, BM48-31, RfGB02, and
324 RhGB07; and Type-3 RBD S-proteins from GX2013, HeB2013, YN2013, and
325 RmYN02. The results show that bACE2$_{R.cor}$ can support receptor binding mediated
326 cell fusion activities of several sarbecovirus S-proteins with Type-1 RBDs (**Fig. 4J**

327 and **K**). However, potent fusion activity was only observed for several S-proteins
328 of viruses from the SARS-CoV-2 clade. Although the SARS-CoV-1 S-protein
329 exhibits only intermediate bACE2$_{R.cor}$-mediated cell-fusion activity, it is
330 nevertheless the most potent within the SARS-CoV-1 clade (**Fig. 4I-K**). Among
331 bACE2$_{R.cor}$ utilizing S-proteins, the BANAL-20-236 S-trimer was found to bind
332 bACE2$_{R.cor}$ in BLI assays, whereas S-trimers of BANAL-20-52, SARS-CoV-2 and
333 SARS-CoV-1 showed no binding to bACE2$_{R.cor}$ **(Fig. 4K** and **Fig. S9B, C, E** and
334 **F)**.

335

336 The Asn38-linked glycan in bACE2$_{R.cor}$ is involved in S-protein binding, a feature
337 observed for the first time between an ACE2 and a sarbecovirus S-protein. To
338 understand the effect of this glycan on S-protein binding, we removed the glycan
339 by introducing a Thr40Ala change (designated as 'bACE2$_{R.cor}$-ΔGLC$_{38}$').
340 bACE2$_{R.cor}$-ΔGLC$_{38}$ appears to support enhanced cell fusion activities for S-
341 proteins capable of utilizing bACE2$_{R.cor}$ **(Fig. 4J-K** and **Fig. S9A, C, E** and **H)**.
342 BLI assay results show that the removal of the Asn38-glycan was able to enhance
343 bACE2$_{R.cor}$ binding by monomeric RBDs and S-trimers of Rc-o319 and BANAL-
344 20-236 in BLI assays (**Fig. S9A, E, J** and **K**), despite that the Asn38-glycan was
345 found involved in the interface formed between bACE2$_{R.cor}$ and Rc-o319-RBD
346 **(Fig. 3E, G** and **I)**. Further, although unable to utilize WT bACE2$_{R.cor}$, the Type-2
347 BtKY72 S-protein was found to utilize bACE2$_{R.cor}$-ΔGLC$_{38}$, albeit only showing
348 very weak cell fusion activity. Consistently, BLI binding result shows that the
349 BtKY72 S-trimer binds bACE2$_{R.cor}$-ΔGLC$_{38}$ with an estimated affinity of 11.8 nM
350 (**Fig. S9H, the second panel)**. These data suggest that the Asn38-linked glycan,
351 likely due to its bulky and branched structure, imposes steric hindrance on S-
352 protein binding.

353

354 **Discussion**

355

356 In this study, our receptor binding and structural analyses show that Rc-o319 S-
357 protein exhibits a clear preference for its cognate bACE2$_{R.cor}$ receptor with marked

358 reduced utilization of *R. sinicus* and *R. affinis* ACE2 receptors. Rc-o319 S-protein
359 showed no utilization of human and pangolin ACE2s. A closer relationship among
360 Asian *Rhinolophus* bats (50) probably allowed Rc-o319 S-protein to cross-bind *R.*
361 *sinicus* and *R. affinis* ACE2s. Previously, it has been shown that weak binding of
362 SARS-CoV-2 S-protein to mouse ACE2 (mACE2) was unable to facilitate
363 effective mouse infection, and increased mACE2 binding was key to effective
364 mouse infection (51). Therefore, weak *R. sinicus* and *R. affinis* ACE2 binding may
365 not allow effective infection of *R. sinicus* and *R. affinis* bats by the Rc-o319 virus.

366

367 Our structural analyses reveal that the Rc-o319 S-trimer adopts two distinct
368 conformations: a locked-1 conformation with fatty-acid bound RBDs and a locked-
369 2 conformation in which those fatty-acid binding pockets are unoccupied. Previous
370 cryo-EM studies of bat sarbecovirus S-trimers have nearly always captured them in
371 locked-2 conformations with and without fatty acid bound (17). Locked-1
372 conformation has only been reported for the bat sarbecovirus WIV1 S-trimer (52).
373 Both locked-1 and locked-2 conformations have been observed for SARS-CoV-1
374 and SARS-CoV-2 S-trimers. The locked-1 conformation appears to be always
375 identified with fatty acid bound, whereas the locked-2 conformation has been
376 resolved with or without fatty acid bound. Interestingly, these two conformations
377 appear to be more difficult to capture for SARS-CoV-1 (25) and SARS-CoV-2 (22,
378 38, 53) S-trimers and their capture often requires deliberate stabilization of the S-
379 trimers. The predominance of locked conformations in bat sarbecovirus S-trimers,
380 versus them being rare conformations in human-infecting sarbecoviruses, has been
381 proposed to reflect likely differences in S-trimer stability (17). We have also
382 proposed that tightly packed S-trimers in locked conformations facilitate viral
383 egress (38). As the preferred conformation for bat sarbecovirus S-proteins, these
384 locked conformations have also been postulated to represent adaptations for fecal-
385 oral transmission and immune evasion in their natural hosts (52, 54).

386

387 Due to residue-31 of bat ACE2 molecules often being a negative charged Asp or
388 Glu, a positively charged LM region, such as $K458_{Rc\text{-}o319}$ (corresponding to
389 $Q493_{SARS2}$), has been noted as an important determinant for specificity towards
390 bACE2 (45). Monomeric BANAL-20-236-RBD, with a K in the LM region, with

391 the ability to bind a variety of bACE2 molecules (54), binds bACE2$_{Ra5538}$ with a
392 moderate affinity of 104 nM (17). For comparison, it binds bACE2$_{R.cor}$ with a
393 much reduced affinity of 937 nM **(Fig. S9K, the top panel)**. SARS-CoV-2-RBD is
394 highly similar to BANAL-20-236, however, with a neutral Q in the LM region,
395 SARS-CoV-2-RBD-Fc binding to bACE2$_{R.cor}$ is too weak to be measured by the
396 BLI assay. With a Q493K$_{SARS2}$ point mutation in LM, SARS-CoV-2-RBD-Fc binds
397 bACE2$_{R.cor}$ in BLI assays (compare **Fig. S8H** and **L**). In addition, SARS-CoV-1-
398 RBD-Fc with the N482K$_{SARS1}$ gained weak bACE2$_{R.cor}$ binding (**Fig. S8K**). These
399 results are consistent with the LM change (K458Q$_{Rc\text{-}o319}$) in the Rc-o319 S-protein,
400 which considerably reduced bACE2$_{R.cor}$ binding (**Fig. 4C**), suggesting that a
401 positive-charged LM region contributes to high-affinity binding towards the
402 bACE2$_{R.cor}$ receptor.

403

404 The Rc-o319-RBD:bACE2$_{R.cor}$ complex structure reveals that Rc-o319-RBD
405 employs a featured beta-loop (BL) structure to bind the bACE2$_{R.cor}$ molecule using
406 a previous unobserved novel interaction pattern. While this manuscript was in
407 preparation, Kosugi et al. reported a cryo-EM structure of the Rc-o319-
408 RBD:bACE2$_{R.cor}$ complex (55), corroborating the interactions we observed and
409 identifying Y463$_{Rc\text{-}o319}$ and S465$_{Rc\text{-}o319}$ in the AL region as critical for bACE2$_{R.cor}$
410 binding. Importantly, beyond these AL-region interactions, we show that the BL
411 and LM regions also govern bACE2$_{R.cor}$ engagement, and that replacing the Rc-
412 o319 BL with the SARS-CoV-2 LL sequence has a substantially greater impact on
413 bACE2$_{R.cor}$ binding than multiple LM mutations (**Fig. 4B** vs **Fig. 4C**and see **Fig.**
414 **S8D** for the K458A$_{Rc\text{-}o319}$ substitution), establishing the BL as a principal
415 determinant of high-affinity binding in Rc-o319 S.

416

417 Our data show that the specialized BL loop co-adapts with the Rc-o319 RBM loop
418 to confer high-affinity binding to its cognate bACE2$_{R.cor}$ receptor, but this co-
419 adaptation renders the RBM-loop incompatible with the SARS-CoV-2 LL region
420 **(Fig. S6C** and **F)**, preventing an introduced LL region from mediating high-affinity
421 hACE2 binding in BLI **(**compare **Fig. 4F** and **G,** compare **Fig. S7C** and **D)**.
422 Conversely, changing SARS-CoV-2 LL to the BL in Rc-o319-RBD completely
423 abolishes hACE2 binding and bACE2$_{R.cor}$ binding (**Fig. S10A** and **E**), likely due to

424 incompatibility between BL and RBM-loop. These observations further suggest
425 that the Rc-o319 BL and RBM-loop are specialized structures adapted for
426 bACE2$_{R.cor}$ binding, and their unique structural features and interactions engaged
427 support classifying the Rc-o319-RBD as a novel Type-4 RBD. However, our data
428 show the specialized BL and RBM-loop of the Rc-o319 RBM severely limit its
429 capacity for high-affinity hACE2 binding, with extensive mutations and insertions
430 in these regions likely required to achieve the binding affinity necessary for cross-
431 species transmission.

432

433 Finally, our results show that, in contrast to the highly efficient utilization of
434 bACE2$_{R.cor}$ by the Rc-o319 S-protein, bACE2$_{R.cor}$ supports only limited usage by
435 selected sarbecovirus S-proteins with Type-1 RBDs. Notably, most of these S-
436 proteins are from viruses that belong to the SARS-CoV-2 clade (Clade 1b),
437 highlighting this clade's extraordinary ability to recognize a broad range of ACE2
438 orthologs. Albeit showing cell fusion activities, most bACE2$_{R.cor}$ utilizing S-
439 proteins show weak binding of bACE2$_{R.cor}$ in BLI assays. Therefore, bACE2$_{R.\mathrm{cor}}$
440 appears to have evolved to permit efficient binding by the S-proteins of highly
441 specific sarbecovirus species. Further, our data show that the Asn38-glycan of
442 bACE2$_{R.cor}$ hinders sarbecovirus S-protein binding, likely further restricting its
443 utilization as a receptor. Interestingly, the Asn38-linked glycan is also located
444 within the binding interfaces of multiple ACE2-utilizing Merbecovirus S-proteins,
445 and is therefore likely to restrict their binding (56, 57).

446

447 In summary, the interaction between the Rc-o319 S-protein, featuring a specialized
448 RBM, and bACE2$_{R.cor}$ reflects a highly specific co-adaptation between virus and
449 host. To enable such adaptation, the RBM of Rc-o319 has diverged substantially
450 from that of the SARS-CoV-2 lineage, to which it is most closely related, resulting
451 in a highly restricted ACE2 specificity. Notably, the RBM is also a major target of
452 immune pressure, as demonstrated by the ongoing evolution of SARS-CoV-2 (58-
453 62). Even though certain SARS-CoV-2 lineage viruses can use bACE2$_{R.cor}$, we still
454 do not know what evolutionary forces, perhaps immune pressure, pushed Rc-o319
455 S toward specialization for its host receptor.

456 ## Materials and Methods

457 **Protein constructs**

458 S gene of Rc-o319 (Taxonomy ID: 694009) was codon-optimized and synthesized
459 by Sangon Biotech (Shanghai, China). The transmembrane domain and C-terminal
460 end of Rc-o319 (AA 1176-1235) were removed before the C-terminus of the
461 coding sequence was fused to a T4 trimerization foldon, an HRV3C cleavage site,
462 an Octo-His tag, and a double strep-tag to allow secretory expression and
463 purification.

464 *Rhinolophus cornutus* (*R.cor*, Genebank: BCG67443.1), human (hACE2,
465 Genebank: BAB40370.1), *Rhinolophus ferrumequinum* (*R.ferr*, Genbank:
466 BAH02663.1) and greater mouse-eared bat *Myotis lucifugus* (*M.luci*, Genbank:
467 XP_023609438.1) ACE genes were synthesized. Pangolin (Pangolin, Genbank:
468 XP_017505752.1), *Rhinolophus affinis* 9479 (*Ra9479*, Genbank: QMQ39227),
469 *Rhinolophus affinis* 787 (*Ra5538*, Genbank: QMQ39222), *Rhinolophus sinicus*
470 WJ2 (*Rs*-WJ2, Genbank: QMQ39202.1), *Rhinolophus sinicus* 1434 (*Rs*1434,
471 Genbank: QMQ39216.1), *Rhinolophus sinicus* 1438 (*Rs*1438, Genbank:
472 QMQ39203.1), *Rhinolophus sinicus* 1446 (*Rs*1446 Genbank: MT394194.1),
473 *Rhinolophus sinicus* 3357 (*Rs*3357 Genbank: AGZ48803.1), *Rhinolophus sinicus*
474 3359 (*Rs*3359 Genbank: QMQ39211.1), *Rhinolophus sinicus* 3366 (*Rs*3366,
475 Genbank: QMQ39215.1) and *Rhinolophus sinicus* 5720 (*Rs*5720, Genbank:
476 MT394182.1) ACE2 gene sequences were from a previous study (63). The
477 peptidase domain and the C-terminal collectrin-like domain of ACE2, bearing a
478 carboxy-terminal Hexa-His tag, was generated for hACE2. Due to the presence of
479 the C-terminal collectrin-like domain, these his-tagged ACE2 (AA 1-731) proteins
480 form dimers. Additionally, the same length of ACE2s were fused to the Fc domain
481 of human IgG with one thrombin site and a GGGG linker in between, resulting in
482 Fc-tagged ACE2.

483 Rc-o319 RBD and variants (AA 293-506), SARS-CoV-2 RBD (AA 319-541),
484 were fused with human IgG Fc domains to generate dimeric RBD-Fc proteins.

485 **Protein expression and purification**

486 Proteins were expressed by transient transfection in Expi293F cells, 1 mg of DNA
487 was transfected into 1 L of cells using Linear Polyethylenimine (PEI) transfection
488 reagent. After transfection, cells were cultured at 33 °C for 4 days for S-proteins, 5
489 days for RBD and ACE2 proteins. For his-tagged S-proteins and RBD proteins, the
490 supernatants were harvested by centrifugation and 25 mM phosphate pH 8.0, 3
491 mM imidazole, 300 mM NaCl, and 0.5 mM PMSF were supplemented.
492 Supernatant was recirculated onto a 5-ml Talon Cobalt column for about 3 times
493 and the column was washed by 100 ml buffer A (25 mM phosphate pH 8.0, 5 mM
494 imidazole, and 300 mM NaCl). Proteins were eluted using a linear gradient with
495 increasing concentration of Buffer B (25 mM phosphate pH 8.0, 500 mM
496 imidazole, and 300 mM NaCl). Eluted protein samples were quality checked by
497 SDS-PAGE, concentrated and buffer-exchanged into PBS using a 100 kDa (for S-
498 proteins) or 10 kDa (for RBD proteins) MWCO Amicon Ultra filtration device
499 (Merck Millipore). The concentrated proteins were frozen in liquid nitrogen and
500 stored at -80 °C.

501 For RBD-Fc and ACE2-Fc proteins, 5 days post-transfection, each culture
502 supernatant was cleared by filtering through a 0.45 μm filter membrane before
503 being loaded onto a 5 mL HiTrap Protein A column (Cytiva). The column was
504 washed by PBS (10 mM Na_2HPO_4 and 1.8 mM KH_2PO_4 pH 7.4, 137 mM NaCl,
505 and 2.7mM KCl). Proteins were eluted using a linear gradient with increasing
506 concentration of a citrate buffer (0.1 M citric acid, pH 3.0). Eluted protein fractions
507 were immediately neutralized with equal volumes of 1.0 M Tris-HCl pH 8.0
508 buffer. RBD-Fc and ACE2-Fc proteins were concentrated, buffer-exchanged into
509 PBS before being frozen and stored at -80 °C.

510 **Biolayer Interferometry (BLI) binding analysis**

511 Binding of Rc-o319 S-proteins or RBDs to ACE2-Fc proteins was assessed using
512 biolayer interferometry (BLI) on an Octet RED 96 instrument (FortéBio, USA).
513 All steps were performed at 25 °C with an orbital shaking speed of 1000 rpm. All
514 reagents were formulated in PBS-TB buffer (PBS with 0.02% v/v Tween-20 and
515 0.1% w/v BSA). Before the experiments, all protein A biosensors were pre-
516 equilibrated in the PBS-TB buffer for 10 min. ACE2-Fc proteins (11 μg/ml) were
517 immobilized onto Protein A biosensors (FortéBio, USA) to a response value of

518 ~1.2 nm. After a 60 s baseline step in PBS-TB, the biosensors immobilized with
519 ACE2-Fc proteins were submerged in the analyte (S-proteins or RBDs) solutions
520 for 300 s to measure association, before being submerged in PBS-TB for 600 s to
521 measure dissociation. Data were reference subtracted and analyzed in the FortéBio
522 Data Analysis Software (FortéBio) by fitting to 1:1 or 2:1 binding models to
523 determine k_{on}, k_{off}, and K_D values as previously described (64). Raw data and fits
524 were plotted using GraphPad Prism 8 (GraphPad Software).

525 Binding of dimeric his-tagged hACE2, pangolin ACE2, and bACE2s to Rc-o319
526 RBD-Fc protein was assessed using the BLI assay. The RBD-Fc proteins (11
527 μg/ml) were loaded onto Protein A biosensors (FortéBio, USA) to a level of ~1.2
528 nm. After a 60 s baseline step in PBS-TB buffer, the biosensors immobilized with
529 RBD-Fc proteins were submerged in the ACE2 protein solutions for 300 s to
530 measure association, before being submerged in PBS-TB for 600 s to measure
531 dissociation. Data were reference subtracted and analyzed in the FortéBio Data
532 Analysis Software.

533 **Cryo-EM grid preparation and data acquisition**

534 Cryo-EM grids were prepared with Rc-o319 S-trimer samples at concentration of
535 1.65 mg/ml. All grids were prepared by applying 3.0 μl of S-trimer solutions
536 directly to glow discharged (15 mA, 30 s) holey carbon grids (Quantifoil Cu mesh
537 300 R1.2/R1.3) before blotting. Cryo-EM grids were blotted for 2.5 s with a blot
538 force of 4, before being plunge-frozen into liquid ethane using a Vitrobot Mark IV
539 (ThermoFisher) at 4 °C and 100% humidity.

540 For Rc-o319 S-proteins, micrographs were collected using the EPU software
541 (Thermo Fisher) on a Titan Krios G3i electron microscope (Thermo Fisher)
542 operated at 300 keV. Micrographs were recorded at a nominal magnification of
543 130,000× on a Falcon 4 direct electron detector coupled to a Selectris-X energy
544 filter set with a slit width of 10 eV and with a defocus range between -0.8 to -2.0
545 μm. Each movie was collected with a dose rate of 25 e^-/pixel/second, and exposed
546 for 2.28 seconds, resulting in a total dose of 50 $e^-/Å^2$ with a calibrated pixel size of
547 0.93 Å.

548 For complex formation, wild-type dimeric Rc-o319 RBD was mixed with dimeric
549 Fc-tagged bACE2$_{R.cor}$ at a 1.2:1 molar ratio, followed by incubation at 4 °C in the

550 presence of 0.01% glutaraldehyde for 20 min. The glutaraldehyde was quenched
551 by adding Tris-HCl to a final concentration of 50 mM. Gel filtration was
552 performed to remove excess RBD on a Superose 6 10/300 GL column (Cytiva)
553 equilibrated in PBS buffer. Complex formation was confirmed by SDS-PAGE, and
554 the Rc-o319-RBD:bACE2$_{R.cor}$ complex peak was collected and concentrated to
555 prepare cryo-EM grids. 3 µL of 6.8mg/mL the RBD-ACE2 complex was mixed
556 with 8 mM 3-[(3-Cholamidopropyl)dimethylammonio]-2-hydroxy-1-
557 propanesulfonate (CHAPSO) before being applied onto glow discharged (15 mA,
558 30 s) Ni-Au-300 mesh R1.2/1.3 grids. Grids were blotted for 2.5 s with a blot force
559 of 5 before being plunge frozen into liquid ethane using a Vitrobot Mark IV
560 (Thermo Fisher Scientific) at 4 °C and 100% humidity. Micrographs were
561 collected on a Titan Krios electron microscope (Thermo Fisher) operated at 300
562 keV using the EPU software (Thermo Fisher). Micrographs were recorded at a
563 nominal magnification of 130,000× on a K3 direct electron detector (Gatan)
564 coupled to a Gatan BioQuantum energy filter set with a slit width of 20 eV
565 (Thermo Fisher) and with a defocus range between -0.8 to -2.0 µm. Each movie
566 was collected with a dose rate of 18.7 e^-/pixel/second, exposed for 1.78 seconds,
567 resulting in a total dose of 50 $e^-/Å^2$ with a calibrated pixel size of 0.65 Å.

568 **Image processing**

569 For dataset processed by the CryoSPARC package (65), particles were picked
570 before 2D classification was performed. Well featured particles from the 2D
571 classification were subjected to *ab initio* 3D classification. Homogeneous
572 Refinement and Local Refinement were applied to the set of particles with good
573 features identified by the *ab initio* 3D classification.

574 For the Rc-o319-RBD:bACE2$_{R.cor}$ complex dataset, data processing was performed
575 mainly using cryoSPARC (65). After patch-motion correction and CTF estimation,
576 micrographs with CTF fit resolution above 6Å were picked by the curate exposures
577 job. Particles were then picked using a blob picker to generate templates for the
578 subsequent template picker. Picked particles were extracted at 3x binning and
579 subjected to 2D classification, *ab initio* reconstruction, and heterogeneous
580 refinement. Particles belongs to classes with high-resolution details were selected
581 for a final round of Topaz picker by the Topaz cross validation job. Picked
582 particles were extracted at 3x binning and subjected to 2D classification, *ab initio*

583 reconstruction, and heterogeneous refinement again. Highly similar classes in
584 heterogeneous refinement showing high-resolution details were combined and re-
585 extracted at 1.5x binning and subjected to non-uniform refinement with
586 optimization of per-group CTF parameter analysis. The CTF-refined particles and
587 volumes were subjected to reference-based motion correction and an extra round of
588 non-uniform refinement to get the final dimeric structure.

589 Due to conformational dynamics in the dimeric RBD-ACE2 complex structure,
590 several local regions were resolved to lower resolution. Local refinement was
591 applied to improve the local resolution at the RBD-ACE2 binding interface.
592 Particles were symmetry expanded, the dynamic parts were masked, before the
593 particles were subtracted through masking. The subtracted particles were imported
594 to perform NU-Refine and local refinement jobs.

595 **Model building and structure refinement**

596 A previous determined SARS-CoV-2 S-trimer structure (PDB ID: 6ZP2) (22) was
597 used as the starting models for the Rc-o319 S-trimer structures. Model building
598 and adjustment were performed manually in Coot 0.9 (66). Steric clash and
599 sidechain rotamer conformations were improved using the Namdinator web server
600 (67). Final structures after additional manual adjustments were refined and
601 validated in PHENIX-1.18.261 (68). The SARS-CoV-2-RBD:hACE2-B^0AT1
602 complex structure (PDB ID: 6M17, EMD-30039) (27, 69) was used as the starting
603 model for the Rc-o319 RBD:bACE2$_{R.cor}$ complex structure. The starting model was
604 fitted in the cryo-EM density in Chimera before manual adjustments were carried
605 out in Coot. The model was refined by multiple rounds of refinement in
606 Namdinator and PHENIX. Data collection and refinement statistics for all the
607 reported structures are provided in Table S1.

608 **GFP-split fusion assay**

609 The split-GFP system based cell-cell fusion assay mediated by the interaction
610 between the S-protein and the ACE2 receptor was previously described (35).
611 Briefly, HEK293T cells transfected with full length S-proteins and pQCXIP-
612 GFP1-10 were prepared as effector cells, while HEK293T cells transfected with
613 bat ACE2 (*R.cor*, *Rs*-WJ2, *Rs*1446, *Rs*1434, *Rs*1438, *Rs*3357, *Rs*3366, *Rs*3359,
614 *Rs*5720, *Ra*9479, *Ra*5538, *R.ferr*, and *M.luci*) or pangolin ACE2 or human ACE2

615 (hACE2) and pQCXIP-BSR-GFP11 served as receptor cells. 24 h after
616 transfection, effector and receptor cells were washed and resuspended in DMEM
617 containing 10% FBS without trypsin treatment, mixed at a 1:1 ratio, and plated at
618 ~2×10^5 cells per well in a 96-well plate. Fluorescence images were recorded at
619 the indicated time points using a Nikon TS2-S-SM fluorescence microscope. The
620 GFP area was quantified with ImageJ. S-protein expression was analyzed via flow
621 cytometry using a SARS-CoV-2 S2 antibody (1:2500 dilution, Sino Biological,
622 40590-T62) and Western blot using an anti-FLAG antibody (1:1000 dilution, Sino
623 Biological, 109143-MM13). The GFP area was normalized to the mean
624 fluorescence intensity of surface S-proteins.

625

Data availability

Cryo-EM density maps and coordinates generated in this study have been deposited in the Electron Microscopy Data Bank (EMDB; www.ebi.ac.uk/emdb/) and the Protein Data Bank (PDB; www.rcsb.org/ with the following accession numbers: Rc-o319 locked-1 S-trimer: EMD-65717 and PDB:9W75; Rc-o319 locked-2 S-trimer: EMD-65718 and PDB: 9W76; Dimeric Rc-o319-RBD:bACE2$_{R.cor}$ complex: EMD-65719 and PDB: 9W77, monomeric Rc-o319-RBD:bACE2$_{R.cor}$ complex: EMD65720 and PDB: 9W78. All data needed to evaluate the conclusions in the paper are present in the paper and/or the Supplementary Materials.

Acknowledgments

We thank the staff of the GIBH-CAS Cryo-EM Facility for their help with cryo-EM sample preparation and data collection. We thank the staff of the Guangzhou Laboratory Cryo-EM Facility for their help with cryo-EM sample data collection. This work was supported by the National Key R&D Program of China (2021YFA1300903 to X.X.); the National Natural Science Foundation of China (82341085 to X.X.); the Emergency Key Program of Guangzhou Laboratory (EKPG21–06 to X.X.); the R&D Program of Guangzhou National Laboratory (SRPG22–002 to X.X. and SRPG22-003 to J.H); the Guangdong Basic and Applied Basic Research Foundation (2021A1515011289 to X.X.); the Science and Technology Planning Project of Guangdong Province, China (2023B1212060050 to X.X., 2023B1212120009 to X.X.); the Basic Research Project of Guangzhou Institutes of Biomedicine and Health, Chinese Academy of Sciences (GIBHBRP24-02 to X.X.); the Natural Science Fund of Guangdong Province (2022A1515110211 to J.W.); the Young Doctoral Starting Sail Project of the Guangzhou Municipal Science and Technology Bureau (2024A04J4197 to J.W., 2024A04J4357 to Y.M.); and the Grants from State Key Laboratory of Respiratory Diseases (SKLRD-Z-202515 to Y.M.). X.X. acknowledges Start-up grants from the Chinese Academy of Sciences.

Author contributions

J.W., Z.L., and Y.M. conceived the study under the direction of X.C. and X.X. J.W. and Z.L. performed the clone design, protein purification and EM-structure

663 determination study; Y.M. performed the cell-cell fusion and FCAS assays; Z. L.
664 and H.Y. performed BLI assays; J.W., B.L., C.N. and X.X. analysied the BLI
665 results; J.W., Z.L., M.L., H.F. and M.Z. helped collect cryo-EM data under the
666 supervision of J.H.and X.X.; Z.L., Zimu Li and J.W. processed cryo-EM data
667 under the supervision of X.X.; J.W. Z.L. and X.X. analyzed cryo-EM structures;
668 J.W., Z.L. and Y.M. prepared the figures under the supervision of X.X.; J.W., Z.L.,
669 Y.M. and X.X. wrote the paper with input from all authors; J.C. and J.H. reviewed
670 and edited the manuscript; X.C. and X.X. supervised the research.
671

672 **Conflict of interest**

673 The authors declare no competing interests.

674

675

References

1. J. S. Peiris, C. M. Chu, V. C. Cheng, K. S. Chan, I. F. Hung, L. L. Poon, K. I. Law, B. S. Tang, T. Y. Hon, C. S. Chan, K. H. Chan, J. S. Ng, B. J. Zheng, W. L. Ng, R. W. Lai, Y. Guan, K. Y. Yuen, H. U. S. S. Group, Clinical progression and viral load in a community outbreak of coronavirus-associated SARS pneumonia: a prospective study. *Lancet* **361**, 1767-1772 (2003).
2. C. Drosten, S. Gunther, W. Preiser, S. van der Werf, H. R. Brodt, S. Becker, H. Rabenau, M. Panning, L. Kolesnikova, R. A. Fouchier, A. Berger, A. M. Burguiere, J. Cinatl, M. Eickmann, N. Escriou, K. Grywna, S. Kramme, J. C. Manuguerra, S. Muller, V. Rickerts, M. Sturmer, S. Vieth, H. D. Klenk, A. D. Osterhaus, H. Schmitz, H. W. Doerr, Identification of a novel coronavirus in patients with severe acute respiratory syndrome. *N Engl J Med* **348**, 1967-1976 (2003).
3. R. A. Fouchier, T. Kuiken, M. Schutten, G. van Amerongen, G. J. van Doornum, B. G. van den Hoogen, M. Peiris, W. Lim, K. Stohr, A. D. Osterhaus, Aetiology: Koch's postulates fulfilled for SARS virus. *Nature* **423**, 240 (2003).
4. J. S. Peiris, Y. Guan, K. Y. Yuen, Severe acute respiratory syndrome. *Nat Med* **10**, S88-97 (2004).
5. S. Temmam, K. Vongphayloth, E. Baquero, S. Munier, M. Bonomi, B. Regnault, B. Douangboubpha, Y. Karami, D. Chretien, D. Sanamxay, V. Xayaphet, P. Paphaphanh, V. Lacoste, S. Somlor, K. Lakeomany, N. Phommavanh, P. Perot, O. Dehan, F. Amara, F. Donati, T. Bigot, M. Nilges, F. A. Rey, S. van der Werf, P. T. Brey, M. Eloit, Bat coronaviruses related to SARS-CoV-2 and infectious for human cells. *Nature* **604**, 330-336 (2022).
6. S. Wacharapluesadee, C. W. Tan, P. Maneeorn, P. Duengkae, F. Zhu, Y. Joyjinda, T. Kaewpom, W. N. Chia, W. Ampoot, B. L. Lim, K. Worachotsueptrakun, V. C. Chen, N. Sirichan, C. Ruchisrisarod, A. Rodpan, K. Noradechanon, T. Phaichana, N. Jantarat, B. Thongnumchaima, C. Tu, G. Crameri, M. M. Stokes, T. Hemachudha, L. F. Wang, Evidence for SARS-CoV-2 related coronaviruses circulating in bats and pangolins in Southeast Asia. *Nat Commun* **12**, 972 (2021).
7. S. Murakami, T. Kitamura, J. Suzuki, R. Sato, T. Aoi, M. Fujii, H. Matsugo, H. Kamiki, H. Ishida, A. Takenaka-Uema, M. Shimojima, T. Horimoto, Detection and Characterization of Bat Sarbecovirus Phylogenetically Related to SARS-CoV-2, Japan. *Emerg Infect Dis* **26**, 3025-3029 (2020).
8. J. F. Drexler, F. Gloza-Rausch, J. Glende, V. M. Corman, D. Muth, M. Goettsche, A. Seebens, M. Niedrig, S. Pfefferle, S. Yordanov, L. Zhelyazkov, U. Hermanns, P. Vallo, A. Lukashev, M. A. Muller, H. Deng, G. Herrler, C. Drosten, Genomic characterization of severe acute respiratory syndrome-related coronavirus in European bats and classification of coronaviruses based on partial RNA-dependent RNA polymerase gene sequences. *J Virol* **84**, 11336-11349 (2010).
9. Y. Tao, S. Tong, Complete Genome Sequence of a Severe Acute Respiratory Syndrome-Related Coronavirus from Kenyan Bats. *Microbiol Resour Announc* **8**, (2019).

10. W. Li, Z. Shi, M. Yu, W. Ren, C. Smith, J. H. Epstein, H. Wang, G. Crameri, Z. Hu, H. Zhang, J. Zhang, J. McEachern, H. Field, P. Daszak, B. T. Eaton, S. Zhang, L. F. Wang, Bats are natural reservoirs of SARS-like coronaviruses. *Science* **310**, 676-679 (2005).
11. X. Y. Ge, J. L. Li, X. L. Yang, A. A. Chmura, G. Zhu, J. H. Epstein, J. K. Mazet, B. Hu, W. Zhang, C. Peng, Y. J. Zhang, C. M. Luo, B. Tan, N. Wang, Y. Zhu, G. Crameri, S. Y. Zhang, L. F. Wang, P. Daszak, Z. L. Shi, Isolation and characterization of a bat SARS-like coronavirus that uses the ACE2 receptor. *Nature* **503**, 535-538 (2013).
12. B. Hu, X. Ge, L. F. Wang, Z. Shi, Bat origin of human coronaviruses. *Virol J* **12**, 221 (2015).
13. H. Zhou, J. Ji, X. Chen, Y. Bi, J. Li, Q. Wang, T. Hu, H. Song, R. Zhao, Y. Chen, M. Cui, Y. Zhang, A. C. Hughes, E. C. Holmes, W. Shi, Identification of novel bat coronaviruses sheds light on the evolutionary origins of SARS-CoV-2 and related viruses. *Cell* **184**, 4380-4391 e4314 (2021).
14. D. Delaune, V. Hul, E. A. Karlsson, A. Hassanin, T. P. Ou, A. Baidaliuk, F. Gambaro, M. Prot, V. T. Tu, S. Chea, L. Keatts, J. Mazet, C. K. Johnson, P. Buchy, P. Dussart, T. Goldstein, E. Simon-Loriere, V. Duong, A novel SARS-CoV-2 related coronavirus in bats from Cambodia. *Nat Commun* **12**, 6563 (2021).
15. S. Alkhovsky, S. Lenshin, A. Romashin, T. Vishnevskaya, O. Vyshemirsky, Y. Bulycheva, D. Lvov, A. Gitelman, SARS-like Coronaviruses in Horseshoe Bats (Rhinolophus spp.) in Russia, 2020. *Viruses* **14**, 113 (2022).
16. H. Guo, A. Li, T. Y. Dong, H. R. Si, B. Hu, B. Li, Y. Zhu, Z. L. Shi, M. Letko, Isolation of ACE2-dependent and -independent sarbecoviruses from Chinese horseshoe bats. *J Virol* **97**, e0039523 (2023).
17. J. Wang, Y. Ma, Z. Li, H. Yuan, B. Liu, Z. Li, M. Su, G. Habib, Y. Liu, L. Fu, P. Wang, M. Li, J. He, J. Chen, P. Zhou, Z. Shi, X. Chen, X. Xiong, SARS-related coronavirus S-protein structures reveal synergistic RBM interactions underpinning high-affinity human ACE2 binding. *Sci Adv* **11**, eadr8772 (2025).
18. H. L. Wells, M. Letko, G. Lasso, B. Ssebide, J. Nziza, D. K. Byarugaba, I. Navarrete-Macias, E. Liang, M. Cranfield, B. A. Han, M. W. Tingley, M. Diuk-Wasser, T. Goldstein, C. K. Johnson, J. A. K. Mazet, K. Chandran, V. J. Munster, K. Gilardi, S. J. Anthony, The evolutionary history of ACE2 usage within the coronavirus subgenus Sarbecovirus. *Virus Evol* **7**, veab007 (2021).
19. J. Zhang, T. Xiao, Y. Cai, B. Chen, Structure of SARS-CoV-2 spike protein. *Curr Opin Virol* **50**, 173-182 (2021).
20. B. J. Bosch, R. van der Zee, C. A. de Haan, P. J. Rottier, The coronavirus spike protein is a class I virus fusion protein: structural and functional characterization of the fusion core complex. *J Virol* **77**, 8801-8811 (2003).
21. S. C. Harrison, Viral membrane fusion. *Nat Struct Mol Biol* **15**, 690-698 (2008).
22. X. Xiong, K. Qu, K. A. Ciazynska, M. Hosmillo, A. P. Carter, S. Ebrahimi, Z. Ke, S. H. W. Scheres, L. Bergamaschi, G. L. Grice, Y. Zhang, C.-N. C.-B. Collaboration, J. A. Nathan, S. Baker, L. C. James, H. E. Baxendale, I. Goodfellow, R. Doffinger, J. A. G. Briggs, A thermostable, closed SARS-CoV-2 spike protein trimer. *Nat Struct Mol Biol* **27**, 934-941 (2020).

23. M. Gui, W. Song, H. Zhou, J. Xu, S. Chen, Y. Xiang, X. Wang, Cryo-electron microscopy structures of the SARS-CoV spike glycoprotein reveal a prerequisite conformational state for receptor binding. *Cell Res* **27**, 119-129 (2017).
24. W. Song, M. Gui, X. Wang, Y. Xiang, Cryo-EM structure of the SARS coronavirus spike glycoprotein in complex with its host cell receptor ACE2. *PLoS Pathog* **14**, e1007236 (2018).
25. X. Zhang, Z. Li, Y. Zhang, Y. Liu, J. Wang, B. Liu, Q. Chen, Q. Wang, L. Fu, P. Wang, X. Zhong, L. Jin, Q. Yan, L. Chen, J. He, J. Zhao, X. Xiong, Disulfide stabilization reveals conserved dynamic features between SARS-CoV-1 and SARS-CoV-2 spikes. *Life Sci Alliance* **6**, e202201796 (2023).
26. F. Li, W. Li, M. Farzan, S. C. Harrison, Structure of SARS coronavirus spike receptor-binding domain complexed with receptor. *Science* **309**, 1864-1868 (2005).
27. R. Yan, Y. Zhang, Y. Li, L. Xia, Y. Guo, Q. Zhou, Structural basis for the recognition of SARS-CoV-2 by full-length human ACE2. *Science* **367**, 1444-1448 (2020).
28. J. Y. Si, Y. M. Chen, Y. H. Sun, M. X. Gu, M. L. Huang, L. L. Shi, X. Yu, X. Yang, Q. Xiong, C. B. Ma, P. Liu, Z. L. Shi, H. Yan, Sarbecovirus RBD indels and specific residues dictating multi-species ACE2 adaptiveness. *Nat Commun* **15**, 8869 (2024).
29. W. Li, C. Zhang, J. Sui, J. H. Kuhn, M. J. Moore, S. Luo, S. K. Wong, I. C. Huang, K. Xu, N. Vasilieva, A. Murakami, Y. He, W. A. Marasco, Y. Guan, H. Choe, M. Farzan, Receptor and viral determinants of SARS-coronavirus adaptation to human ACE2. *EMBO J* **24**, 1634-1643 (2005).
30. P. Zhou, X. L. Yang, X. G. Wang, B. Hu, L. Zhang, W. Zhang, H. R. Si, Y. Zhu, B. Li, C. L. Huang, H. D. Chen, J. Chen, Y. Luo, H. Guo, R. D. Jiang, M. Q. Liu, Y. Chen, X. R. Shen, X. Wang, X. S. Zheng, K. Zhao, Q. J. Chen, F. Deng, L. L. Liu, B. Yan, F. X. Zhan, Y. Y. Wang, G. F. Xiao, Z. L. Shi, A pneumonia outbreak associated with a new coronavirus of probable bat origin. *Nature* **579**, 270-273 (2020).
31. P. Han, C. Su, Y. Zhang, C. Bai, A. Zheng, C. Qiao, Q. Wang, S. Niu, Q. Chen, Y. Zhang, W. Li, H. Liao, J. Li, Z. Zhang, H. Cho, M. Yang, X. Rong, Y. Hu, N. Huang, J. Yan, Q. Wang, X. Zhao, G. F. Gao, J. Qi, Molecular insights into receptor binding of recent emerging SARS-CoV-2 variants. *Nat Commun* **12**, 6103 (2021).
32. J. M. Crook, I. Murphy, D. P. Carter, S. T. Pullan, M. Carroll, R. Vipond, A. A. Cunningham, D. Bell, Metagenomic identification of a new sarbecovirus from horseshoe bats in Europe. *Scientific Reports* **11**, 14723 (2021).
33. W. Markotter, M. Geldenhuys, P. Jansen van Vuren, A. Kemp, M. Mortlock, A. Mudakikwa, L. Nel, J. Nziza, J. Paweska, J. Weyer, Paramyxo- and Coronaviruses in Rwandan Bats. *Trop Med Infect Dis* **4**, 99 (2019).
34. Y. Hu, K. Liu, P. Han, Z. Xu, A. Zheng, X. Pan, Y. Jia, C. Su, L. Tang, L. Wu, B. Bai, X. Zhao, D. Tian, Z. Chen, J. Qi, Q. Wang, G. F. Gao, Host range and structural analysis of bat-origin RshSTT182/200 coronavirus binding to human ACE2 and its animal orthologs. *EMBO J*, e111737 (2022).
35. Y. Ma, P. Li, Y. Hu, T. Qiu, L. Wang, H. Lu, K. Lv, M. Xu, J. Zhuang, X. Liu, S. He, B. He, S. Liu, L. Liu, Y. Wang, X. Yue, Y. Zhai, W. Luo, H. Mai, Y. Kuang, S. Chen, F. Ye, N. Zhou, W. Zhao, J. Chen, S. Chen, X. Xiong, M. Shi, J.-A. Pan, Y.-Q. Chen, Spike

805 substitution T813S increases Sarbecovirus fusogenicity by enhancing the usage of
806 TMPRSS2. *PLOS Pathogens* **19**, e1011123 (2023).
807 36. Y. Cai, J. Zhang, T. Xiao, H. Peng, S. M. Sterling, R. M. Walsh, Jr., S. Rawson, S. Rits-
808 Volloch, B. Chen, Distinct conformational states of SARS-CoV-2 spike protein.
809 *Science* **369**, 1586-1592 (2020).
810 37. Z. Ke, J. Oton, K. Qu, M. Cortese, V. Zila, L. McKeane, T. Nakane, J. Zivanov, C. J.
811 Neufeldt, B. Cerikan, J. M. Lu, J. Peukes, X. Xiong, H. G. Krausslich, S. H. W.
812 Scheres, R. Bartenschlager, J. A. G. Briggs, Structures and distributions of SARS-
813 CoV-2 spike proteins on intact virions. *Nature* **588**, 498-502 (2020).
814 38. K. Qu, Q. Chen, K. A. Ciazynska, B. Liu, X. Zhang, J. Wang, Y. He, J. Guan, J. He, T.
815 Liu, X. Zhang, A. P. Carter, X. Xiong, J. A. G. Briggs, Engineered disulfide reveals
816 structural dynamics of locked SARS-CoV-2 spike. *PLoS Pathog* **18**, e1010583
817 (2022).
818 39. C. Toelzer, K. Gupta, S. K. N. Yadav, U. Borucu, A. D. Davidson, M. Kavanagh
819 Williamson, D. K. Shoemark, F. Garzoni, O. Staufer, R. Milligan, J. Capin, A. J.
820 Mulholland, J. Spatz, D. Fitzgerald, I. Berger, C. Schaffitzel, Free fatty acid binding
821 pocket in the locked structure of SARS-CoV-2 spike protein. *Science* **370**, 725-730
822 (2020).
823 40. S. Zhang, S. Qiao, J. Yu, J. Zeng, S. Shan, L. Tian, J. Lan, L. Zhang, X. Wang, Bat and
824 pangolin coronavirus spike glycoprotein structures provide insights into SARS-CoV-
825 2 evolution. *Nat Commun* **12**, 1607 (2021).
826 41. J. Ma, D. Su, Y. Sun, X. Huang, Y. Liang, L. Fang, Y. Ma, W. Li, P. Liang, S. Zheng,
827 Cryo-electron Microscopy Structure of S-Trimer, a Subunit Vaccine Candidate for
828 COVID-19. *J Virol* **95**, 10.1128/jvi.00194-00121 (2021).
829 42. A. Rosa, V. E. Pye, C. Graham, L. Muir, J. Seow, K. W. Ng, N. J. Cook, C. Rees-Spear,
830 E. Parker, M. S. Dos Santos, C. Rosadas, A. Susana, H. Rhys, A. Nans, L. Masino, C.
831 Roustan, E. Christodoulou, R. Ulferts, A. G. Wrobel, C. E. Short, M. Fertleman, R. W.
832 Sanders, J. Heaney, M. Spyer, S. Kjær, A. Riddell, M. H. Malim, R. Beale, J. I.
833 MacRae, G. P. Taylor, E. Nastouli, M. J. van Gils, P. B. Rosenthal, M. Pizzato, M. O.
834 McClure, R. S. Tedder, G. Kassiotis, L. E. McCoy, K. J. Doores, P. Cherepanov, SARS-
835 CoV-2 can recruit a heme metabolite to evade antibody immunity. *Sci Adv* **7**,
836 eabg7607 (2021).
837 43. S. L. Freeman, A. S. F. Oliveira, A. E. Gallio, A. Rosa, M. K. Simitakou, C. J. Arthur, A.
838 J. Mulholland, P. Cherepanov, E. L. Raven, Heme binding to the SARS-CoV-2 spike
839 glycoprotein. *J Biol Chem* **299**, 105014 (2023).
840 44. J. Lee, S. K. Zepeda, Y. J. Park, A. L. Taylor, J. Quispe, C. Stewart, E. M. Leaf, C.
841 Treichel, D. Corti, N. P. King, T. N. Starr, D. Veesler, Broad receptor tropism and
842 immunogenicity of a clade 3 sarbecovirus. *Cell Host Microbe* **31**, 1961-1973 e1911
843 (2023).
844 45. F. Li, Structural analysis of major species barriers between humans and palm civets
845 for severe acute respiratory syndrome coronavirus infections. *J Virol* **82**, 6984-6991
846 (2008).
847 46. B. Dadonaite, J. Brown, T. E. McMahon, A. G. Farrell, M. D. Figgins, D. Asarnow, C.
848 Stewart, J. Lee, J. Logue, T. Bedford, B. Murrell, H. Y. Chu, D. Veesler, J. D. Bloom,

Spike deep mutational scanning helps predict success of SARS-CoV-2 clades. *Nature* **631**, 617-626 (2024).

47. W. T. Harvey, A. M. Carabelli, B. Jackson, R. K. Gupta, E. C. Thomson, E. M. Harrison, C. Ludden, R. Reeve, A. Rambaut, C.-G. U. Consortium, S. J. Peacock, D. L. Robertson, SARS-CoV-2 variants, spike mutations and immune escape. *Nat Rev Microbiol* **19**, 409-424 (2021).
48. M. McCallum, A. De Marco, F. A. Lempp, M. A. Tortorici, D. Pinto, A. C. Walls, M. Beltramello, A. Chen, Z. Liu, F. Zatta, S. Zepeda, J. di Iulio, J. E. Bowen, M. Montiel-Ruiz, J. Zhou, L. E. Rosen, S. Bianchi, B. Guarino, C. S. Fregni, R. Abdelnabi, S. C. Foo, P. W. Rothlauf, L. M. Bloyet, F. Benigni, E. Cameroni, J. Neyts, A. Riva, G. Snell, A. Telenti, S. P. J. Whelan, H. W. Virgin, D. Corti, M. S. Pizzuto, D. Veesler, N-terminal domain antigenic mapping reveals a site of vulnerability for SARS-CoV-2. *Cell* **184**, 2332-2347 e2316 (2021).
49. H. Yuan, J. Wang, Y. Ma, Z. Li, X. Gao, G. Habib, B. Liu, J. Chen, J. He, P. Zhou, Z. L. Shi, X. Chen, X. Xiong, Structures and receptor binding activities of merbecovirus spike proteins reveal key signatures for human DPP4 adaptation. *Sci Adv* **11**, eadv7296 (2025).
50. A. Chornelia, A. C. Hughes, The evolutionary history and ancestral biogeographic range estimation of old-world Rhinolophidae and Hipposideridae (Chiroptera). *BMC Ecol Evol* **22**, 112 (2022).
51. H. Shuai, J. F. Chan, T. T. Yuen, C. Yoon, J. C. Hu, L. Wen, B. Hu, D. Yang, Y. Wang, Y. Hou, X. Huang, Y. Chai, C. C. Chan, V. K. Poon, L. Lu, R. Q. Zhang, W. M. Chan, J. D. Ip, A. W. Chu, Y. F. Hu, J. P. Cai, K. H. Chan, J. Zhou, S. Sridhar, B. Z. Zhang, S. Yuan, A. J. Zhang, J. D. Huang, K. K. To, K. Y. Yuen, H. Chu, Emerging SARS-CoV-2 variants expand species tropism to murines. *EBioMedicine* **73**, 103643 (2021).
52. F. R. Hills, A. R. Eruera, J. Hodgkinson-Bean, F. Jorge, R. Easingwood, S. H. J. Brown, J. C. Bouwer, Y. P. Li, L. N. Burga, M. Bostina, Variation in structural motifs within SARS-related coronavirus spike proteins. *PLoS Pathog* **20**, e1012158 (2024).
53. T. Zhou, Y. Tsybovsky, J. Gorman, M. Rapp, G. Cerutti, G. Y. Chuang, P. S. Katsamba, J. M. Sampson, A. Schon, J. Bimela, J. C. Boyington, A. Nazzari, A. S. Olia, W. Shi, M. Sastry, T. Stephens, J. Stuckey, I. T. Teng, P. Wang, S. Wang, B. Zhang, R. A. Friesner, D. D. Ho, J. R. Mascola, L. Shapiro, P. D. Kwong, Cryo-EM Structures of SARS-CoV-2 Spike without and with ACE2 Reveal a pH-Dependent Switch to Mediate Endosomal Positioning of Receptor-Binding Domains. *Cell Host Microbe* **28**, 867-879 e865 (2020).
54. X. Ou, G. Xu, P. Li, Y. Liu, F. Zan, P. Liu, J. Hu, X. Lu, S. Dong, Y. Zhou, Z. Mu, Z. Wu, J. Wang, Q. Jin, P. Liu, J. Lu, X. Wang, Z. Qian, Host susceptibility and structural and immunological insight of S proteins of two SARS-CoV-2 closely related bat coronaviruses. *Cell Discov* **9**, 78 (2023).
55. Y. Kosugi, K. Matsumoto, S. Lytras, A. Plianchaisuk, J. E. Tolentino, S. Fujita, M. S. Yo, C. Luo, Y. Kim, W. Shihoya, J. Ito, O. Nureki, K. Sato, Molecular basis of sarbecovirus evolution and receptor tropism in natural hosts, potential intermediate hosts, and humans. *Cell Rep* **44**, 116220 (2025).

892 56. Y. J. Park, C. Liu, J. Lee, J. T. Brown, C. B. Ma, P. Liu, R. Gen, Q. Xiong, S. K. Zepeda,
893 C. Stewart, A. Addetia, C. J. Craig, M. A. Tortorici, A. N. Alshukairi, T. N. Starr, H. Yan,
894 D. Veesler, Molecular basis of convergent evolution of ACE2 receptor utilization
895 among HKU5 coronaviruses. *Cell* **188**, 1711-1728 e1721 (2025).
896 57. J. Chen, W. Zhang, Y. Li, C. Liu, T. Dong, H. Chen, C. Wu, J. Su, B. Li, W. Zhang, B.
897 Hu, J. Jia, C. B. Ma, Y. Zhu, X. He, A. Li, K. Pan, H. Lin, Z. Guo, C. Li, L. Zhang, H. Yan,
898 P. Zhou, W. Peng, Z. L. Shi, Bat-infecting merbecovirus HKU5-CoV lineage 2 can use
899 human ACE2 as a cell entry receptor. *Cell* **188**, 1729-1742 e1716 (2025).
900 58. B. Liu, X. Niu, Y. Deng, Z. Zhang, Y. Wang, X. Gao, H. Liang, Z. Li, Q. Wang, Y. Cheng,
901 Q. Chen, S. Huang, Y. Pan, M. Su, X. Lin, C. Niu, Y. Chen, W. Yang, Y. Zhang, Q. Yan,
902 J. He, J. Zhao, L. Chen, X. Xiong, An unconventional VH1-2 antibody tolerates
903 escape mutations and shows an antigenic hotspot on SARS-CoV-2 spike. *Cell Rep*
904 **43**, 114265 (2024).
905 59. Q. Yan, X. Gao, B. Liu, R. Hou, P. He, Y. Ma, Y. Zhang, Y. Zhang, Z. Li, Q. Chen, J.
906 Wang, X. Huang, H. Liang, H. Zheng, Y. Yao, X. Chen, X. Niu, J. He, L. Chen, J. Zhao,
907 X. Xiong, Antibodies utilizing VL6-57 light chains target a convergent cryptic epitope
908 on SARS-CoV-2 spike protein and potentially drive the genesis of Omicron variants.
909 *Nat Commun* **15**, 7585 (2024).
910 60. P. He, B. Liu, X. Gao, Q. Yan, R. Pei, J. Sun, Q. Chen, R. Hou, Z. Li, Y. Zhang, J. Zhao,
911 H. Sun, B. Feng, Q. Wang, H. Yi, P. Hu, P. Li, Y. Zhang, Z. Chen, X. Niu, X. Zhong, L.
912 Jin, X. Liu, K. Qu, K. A. Ciazynska, A. P. Carter, J. A. G. Briggs, J. Chen, J. Liu, X. Chen,
913 J. He, L. Chen, X. Xiong, SARS-CoV-2 Delta and Omicron variants evade population
914 antibody response by mutations in a single spike epitope. *Nat Microbiol* **7**, 1635-
915 1649 (2022).
916 61. H. Yu, B. Liu, Y. Zhang, X. Gao, Q. Wang, H. Xiang, X. Peng, C. Xie, Y. Wang, P. Hu, J.
917 Shi, Q. Shi, P. Zheng, C. Feng, G. Tang, X. Liu, L. Guo, X. Lin, J. Li, C. Liu, Y. Huang, N.
918 Yang, Q. Chen, Z. Li, M. Su, Q. Yan, R. Pei, X. Chen, L. Liu, F. Hu, D. Liang, B. Ke, C.
919 Ke, F. Li, J. He, M. Wang, L. Chen, X. Xiong, X. Tang, Somatically hypermutated
920 antibodies isolated from SARS-CoV-2 Delta infected patients cross-neutralize
921 heterologous variants. *Nat Commun* **14**, 1058 (2023).
922 62. B. Chen, M. Farzan, H. Choe, SARS-CoV-2 spike protein: structure, viral entry and
923 variants. *Nat Rev Microbiol* **23**, 455-468 (2025).
924 63. H. Guo, B. J. Hu, X. L. Yang, L. P. Zeng, B. Li, S. Y. Ouyang, Z. L. Shi, Evolutionary
925 Arms Race between Virus and Host Drives Genetic Diversity in Bat Severe Acute
926 Respiratory Syndrome-Related Coronavirus Spike Genes. *J Virol* **94**, (2020).
927 64. G. W. Carnell, K. A. Ciazynska, D. A. Wells, X. Xiong, E. T. Aguinam, S. H.
928 McLaughlin, D. Mallery, S. Ebrahimi, L. Ceron-Gutierrez, B. Asbach, S. Einhauser, R.
929 Wagner, L. C. James, R. Doffinger, J. L. Heeney, J. A. G. Briggs, SARS-CoV-2 Spike
930 Protein Stabilized in the Closed State Induces Potent Neutralizing Responses. *J Virol*
931 **95**, e0020321 (2021).
932 65. A. Punjani, J. L. Rubinstein, D. J. Fleet, M. A. Brubaker, cryoSPARC: algorithms for
933 rapid unsupervised cryo-EM structure determination. *Nat Methods* **14**, 290-296
934 (2017).

935 66. P. Emsley, B. Lohkamp, W. G. Scott, K. Cowtan, Features and development of Coot.
936 *Acta Crystallogr D Biol Crystallogr* **66**, 486-501 (2010).
937 67. R. T. Kidmose, J. Juhl, P. Nissen, T. Boesen, J. L. Karlsen, B. P. Pedersen,
938 Namdinator - automatic molecular dynamics flexible fitting of structural models
939 into cryo-EM and crystallography experimental maps. *IUCrJ* **6**, 526-531 (2019).
940 68. P. V. Afonine, B. K. Poon, R. J. Read, O. V. Sobolev, T. C. Terwilliger, A. Urzhumtsev,
941 P. D. Adams, Real-space refinement in PHENIX for cryo-EM and crystallography.
942 *Acta Crystallogr D Struct Biol* **74**, 531-544 (2018).
943 69. J. Buchrieser, J. Dufloo, M. Hubert, B. Monel, D. Planas, M. M. Rajah, C. Planchais,
944 F. Porrot, F. Guivel-Benhassine, S. Van der Werf, N. Casartelli, H. Mouquet, T. Bruel,
945 O. Schwartz, Syncytia formation by SARS-CoV-2-infected cells. *EMBO J* **39**, e106267
946 (2020).

947

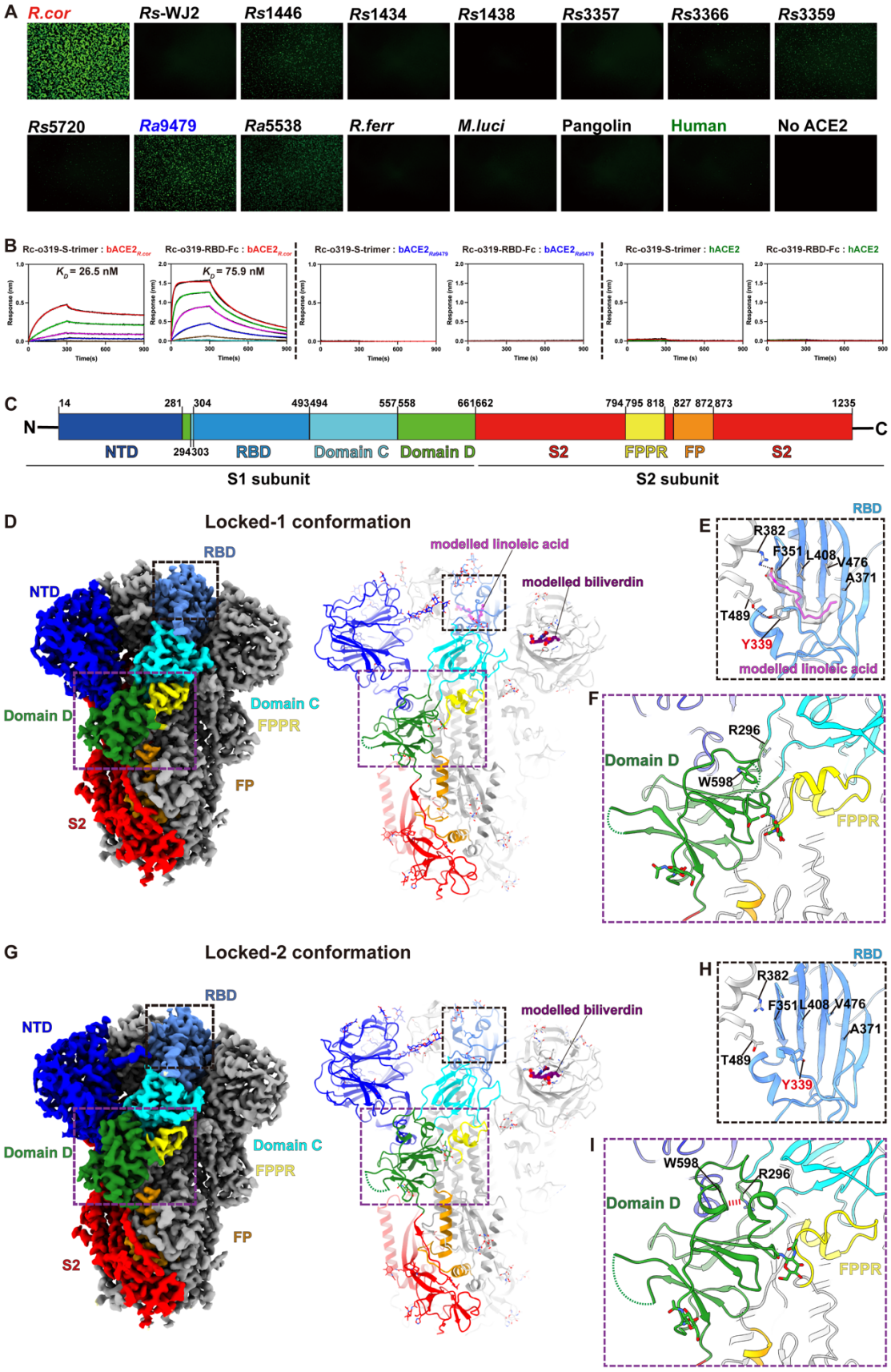
A
R.cor
Rs-WJ2
Rs1446
Rs1434
Rs1438
Rs3357
Rs3366
Rs3359
Rs5720
Ra9479
Ra5538
R.ferr
M.luci
Pangolin
Human
No ACE2
B
Rc-o319-S-trimer : bACE2R.cor
Rc-o319-RBD-Fc : bACE2R.cor
Rc-o319-S-trimer : bACE2Ra9479
Rc-o319-RBD-Fc : bACE2Ra9479
Rc-o319-S-trimer : hACE2
Rc-o319-RBD-Fc : hACE2
KD = 26.5 nM
KD = 75.9 nM
Response (nm)
Time(s)
C
N
C
14
281
304
294
303
493
494
557
558
661
662
794
795
818
827
872
873
1235
NTD
RBD
Domain C
Domain D
S2
FPPR
FP
S2
S1 subunit
S2 subunit
D
Locked-1 conformation
RBD
NTD
Domain D
Domain C
FPPR
FP
S2
modelled linoleic acid
modelled biliverdin
E
RBD
R382
F351
L408
V476
A371
T489
Y339
modelled linoleic acid
F
R296
Domain D
W598
FPPR
G
Locked-2 conformation
RBD
NTD
Domain D
Domain C
FPPR
FP
S2
modelled biliverdin
H
RBD
R382
F351
L408
V476
A371
T489
Y339
I
W598
R296
Domain D
FPPR

949 **Figure 1. Rc-o319 S-protein utilizes a narrow range of *Rhinolophus* bat ACE2**
950 **orthologs as receptors and adopts two locked, 3-RBD-down conformations.**

951 **(A)** Cell-cell fusion assays using receptor cells expressing bat, pangolin or human
952 ACE2 molecules and effector cells expressing the Rc-o319 S-proteins. Fused cells
953 show GFP signals. Representative images of cell-cell fusion captured at 6 hours
954 post-transfection are shown. Scale bar, 500 μm. **(B)** Binding of Rc-o319 S-trimer
955 to immobilized, dimeric bACE2$_{R.cor}$, hACE2 and bACE2$_{Ra9479}$ as assessed by BLI
956 assays. **(C)** A schematic representation showing the eight functional domains or
957 regions of Rc-o319 S-protein. **(D)** Cryo-EM density and associated molecular
958 model showing the overall architecture of a Rc-o319 S-trimer in a locked-1
959 conformation. **(E)** Lipid binding pocket in the RBD of locked-1 Rc-o319 S-trimer.
960 Modeled linoleic acid (magenta) interacts with the shown hydrophobic residues of
961 the lipid binding pocket. Salt bridge and hydrogen bond are shown as dashed lines.
962 **(F)** Structure of the Domain D region in the locked-1 Rc-o319 S-trimer. Consistent
963 with a locked conformation, the fusion peptide proximal region (FPPR) is ordered.
964 Residues 580-605$_{Rc\text{-}o319}$ form a large disordered loop in the locked-1 conformation.
965 **(G)** Cryo-EM density and associated molecular model showing the overall
966 architecture of a locked-2 Rc-o319 S-trimer. **(H)** The RBD lipid binding pocket is
967 empty with Y339$_{Rc\text{-}o319}$ side-chain reorientated in the locked-2 conformation. **(I)**
968 Residues 580-605$_{Rc\text{-}o319}$ refold and form an ordered structure. A stabilizing cation-
969 π interaction (red dashed line) is formed between Domain D residue W598$_{Rc\text{-}o319}$
970 and Domain C-D junction residue R296$_{Rc\text{-}o319}$.

971

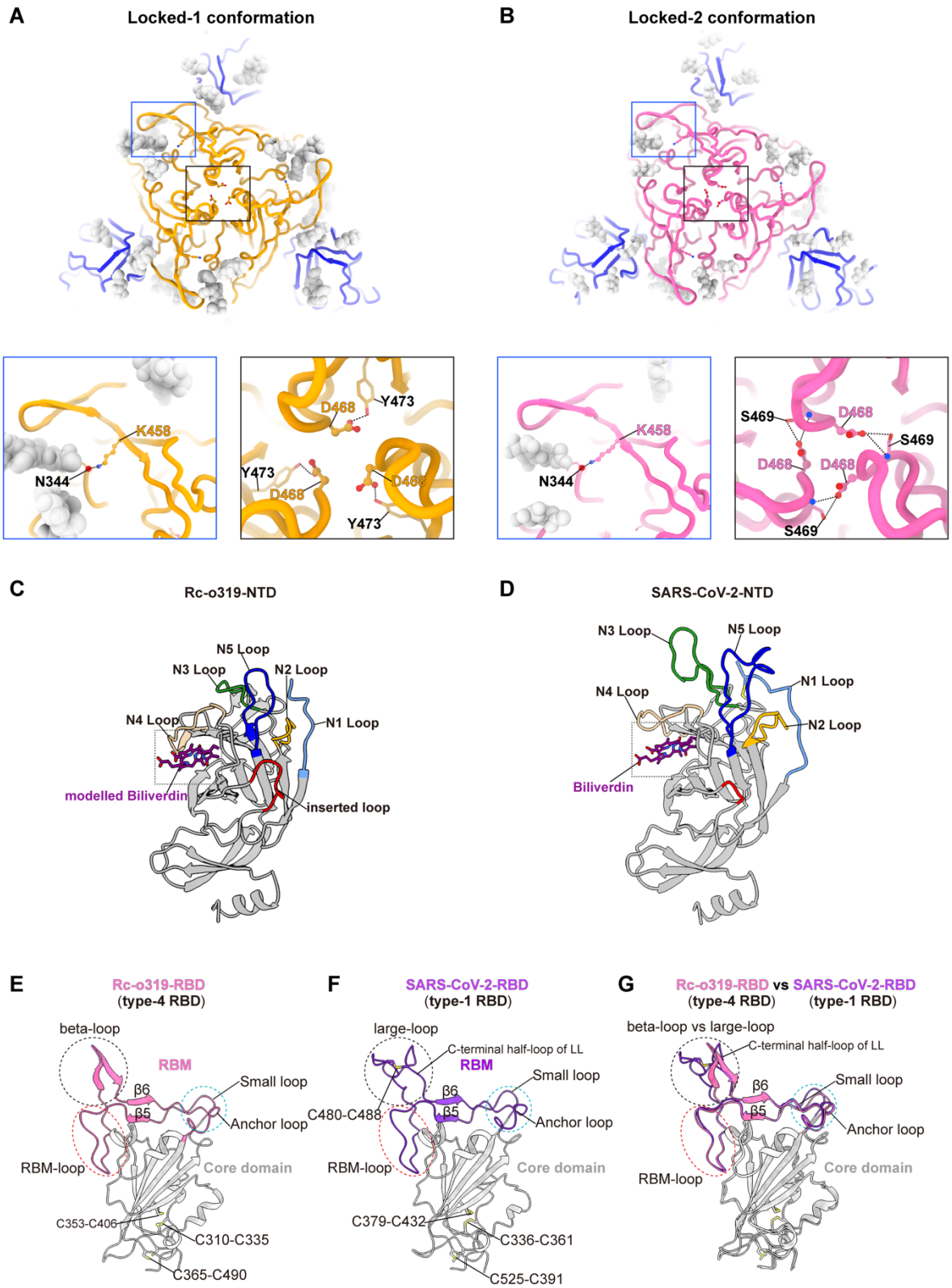
A
Locked-1 conformation
K458
N344
D468
Y473
Y473
D468
D468
Y473
B
Locked-2 conformation
K458
N344
S469
D468
S469
D468
D468
S469
C
Rc-o319-NTD
N5 Loop
N3 Loop
N2 Loop
N4 Loop
N1 Loop
modelled Biliverdin
inserted loop
D
SARS-CoV-2-NTD
N3 Loop
N5 Loop
N1 Loop
N4 Loop
N2 Loop
Biliverdin
E
Rc-o319-RBD
(type-4 RBD)
beta-loop
RBM
β6
β5
Small loop
Anchor loop
RBM-loop
Core domain
C353-C406
C310-C335
C365-C490
F
SARS-CoV-2-RBD
(type-1 RBD)
large-loop
C-terminal half-loop of LL
RBM
Small loop
β6
β5
C480-C488
Anchor loop
RBM-loop
Core domain
C379-C432
C336-C361
C525-C391
G
Rc-o319-RBD vs SARS-CoV-2-RBD
(type-4 RBD) (type-1 RBD)
beta-loop vs large-loop
C-terminal half-loop of LL
Small loop
β6
β5
Anchor loop
RBM-loop
Core domain

973 **Figure 2. Rc-o319 S-trimer structures reveal an RBD featuring a novel RBM**
974 **and an NTD with altered loops.**

975 **(A-B)** Topviews of locked-1 and locked-2 Rc-o319 S-trimer structures. N-linked
976 glycans are shown as light gray spheres. NTDs are colored blue, RBDs are colored
977 orange (locked-1, A) or pink (locked-2, B). The lower panels show intra- or inter-
978 protomer interactions involving RBD residues. $K458_{Rc\text{-}o319}$ forms an inter-protomer
979 hydrogen bond with $N344_{Rc\text{-}o319}$ of an RBD of a neighboring protomer in both
980 locked-1 and locked-2 S-trimers. In the locked-1 conformation, $D468_{Rc\text{-}o319}$ forms
981 an intra-protomer hydrogen bond with $Y473_{Rc\text{-}o319}$; in the locked-2 conformation,
982 $D468_{Rc\text{-}o319}$ instead mediates two inter-protomer hydrogen bonds with $S469_{Rc\text{-}o319}$
983 of an adjacent protomer. **(C-D)** Comparison of Rc-o319 (C) and SARS-CoV-2 (D)
984 N-terminal domain (NTD) structures. The five highly variable NTD loops (N1-N5)
985 are shown in the Rc-o319 and SARS-CoV-2 (PDB: 7XU4) NTD structures. A
986 four-amino-acid residue insertion is highlighted in the Rc-o319 NTD in red. **(E)**
987 The structure of the Rc-o319 RBD. The receptor binding motif (RBM) of the RBD
988 is colored pink and the core of the RBD is colored gray. Disulfide bonds within the
989 RBD are indicated. Featured structural elements, beta-Loop (BL), small loop (SL),
990 Lamella (LM) sheets, β5 and β6, and the large RBM loop are indicated. **(E-G)** For
991 comparison, the SARS-CoV-2 RBD (PDB:7XU4) is shown (F) and superposed on
992 the Rc-o319 RBD structure (E).

993

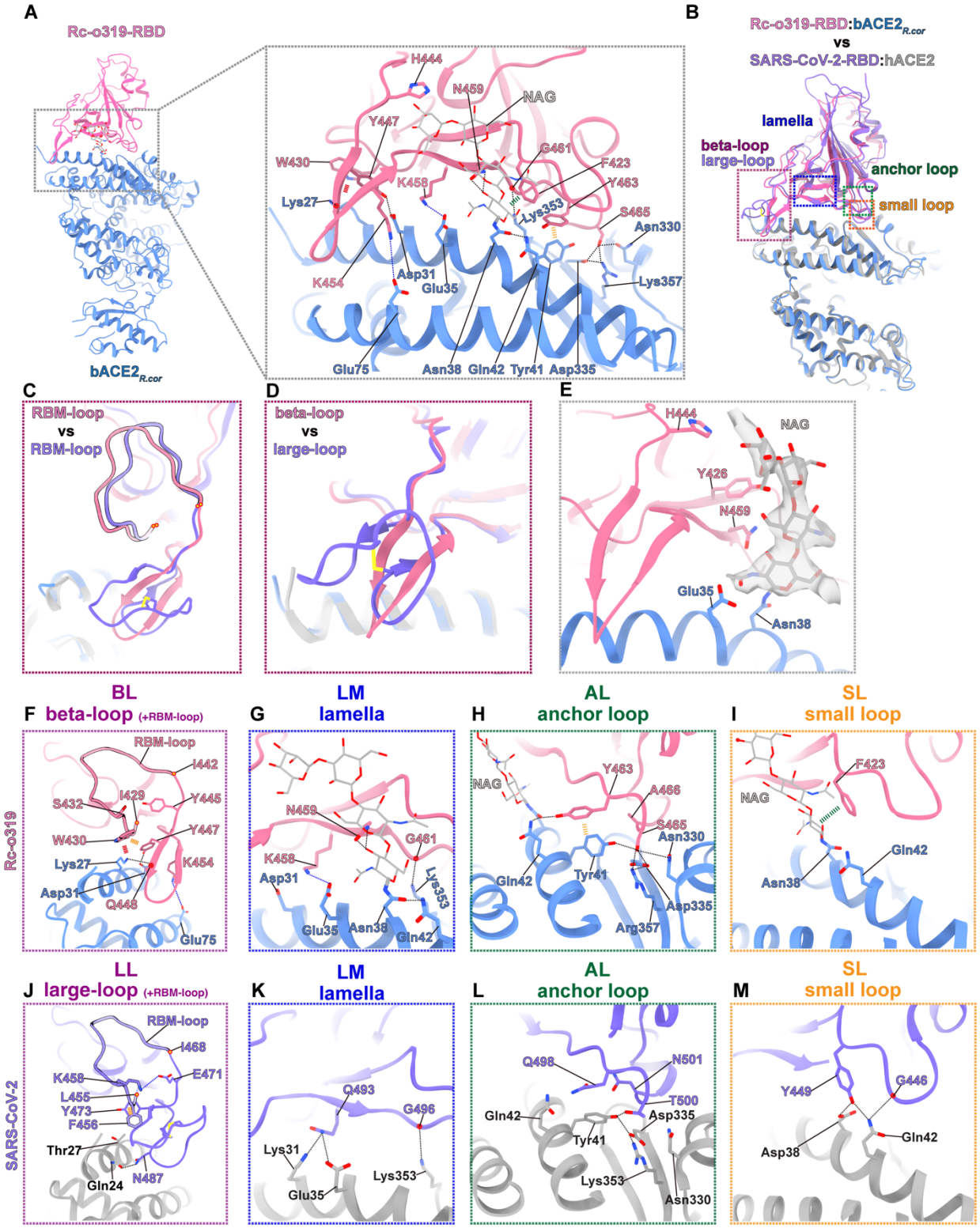

Figure 3. Cryo-EM structure of the Rc-o319-RBD:bACE2$_{R.cor}$ complex with a detailed comparison of RBD:ACE2 interactions versus those in the SARS-CoV-2-RBD:hACE2 complex.

998 **(A)** Molecular structure of a monomeric Rc-o319-RBD:bACE2$_{R.cor}$ complex
999 extracted from the dimeric Rc-o319-RBD:bACE2$_{R.cor}$ complex structure resolved
1000 by cryo-EM (see Figure S1). Detailed interactions formed between the Rc-o319-
1001 RBD and bACE2$_{R.cor}$ are shown with hydrogen bonds and salt bridges shown as
1002 dashed lines. **(B)** Superposition of the Rc-o319-RBD:bACE2$_{R.cor}$ and SARS-CoV-
1003 2-RBD:hACE2 complex structures. The interface areas between the RBD and
1004 ACE2 in the two structures are divided into four regions: beta-loop (BL in Rc-
1005 o319-RBD)/large-loop (LL in SARS-CoV-2-RBD) (purple box), lamella (LM,
1006 blue box), anchor-loop (AL, green box), and small-loop (SL, orange box). **(C-D)**
1007 Comparison of the Rc-o319 RBM-loop and beta-loop (BL) with the RBM-loop and
1008 large-loop (LL) of SARS-CoV-2. **(E)** An N-linked glycan (shown in grey stick
1009 representation overlayed with white cryo-EM density) attached to Asn38 of
1010 bACE2$_{R.cor}$ is involved in the binding interface with Rc-o319-RBD, representing a
1011 unique structural feature. **(F-I)** Detailed interactions identified in the beta-
1012 loop+RBM-loop (BL, purple box), lamella (LM, blue box), anchor-loop (AL,
1013 green box), and small-loop (SL, orange box) regions of the interface between Rc-
1014 o319-RBD and bACE2$_{R.cor}$. **(J-M)** For comparison, detailed interactions are shown
1015 for the corresponding regions in the interface between SARS-CoV-2-RBD and
1016 hACE2. Hydrogen bonds, pi-pi (sugar-pi) interactions and cation-pi interactions
1017 are indicated by black, yellow (green) and red dashed lines, respectively.

1018

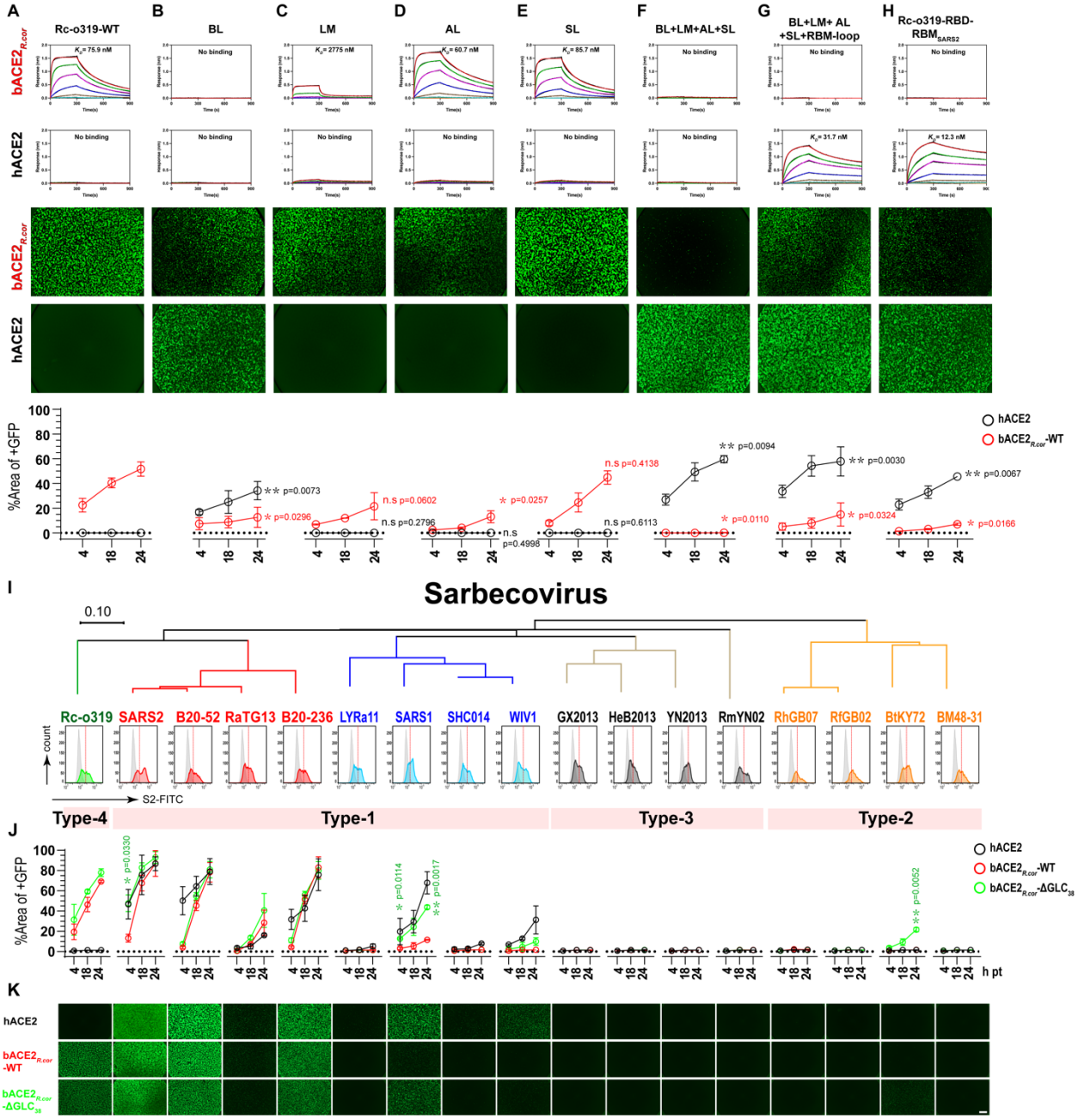

Figure 4. ACE2 utilization by wild-type and variant Rc-o319 S-proteins and bACE2$_{R.cor}$ utilization by different sarbecoviruses S-proteins.

(A-H) Top two panels, binding of bACE2$_{R.cor}$ and hACE2 by wild-type (WT) and variant Rc-o319-RBD-Fc proteins as assessed by BLI assays. Dimeric Rc-o319-RBD-Fc proteins were immobilized on the BLI sensors and tested binding against dimeric *Rhinolophus cornutus* bat ACE2 (bACE2$_{R.cor}$) or hACE2 protein as the analyte in solution. bACE2$_{R.cor}$ and hACE2 were three-fold serial diluted from 3000 to 4.1 nM. K_D values estimated from each binding experiment are shown

1028 alongside the corresponding binding curves. Lower two panels, Representative
1029 images of cell-cell fusion captured at 12 hours post-transfection are shown. Scale
1030 bar, 500 μm. Effector cells expressing WT or variant Rc-o319 S-proteins were
1031 tested against receptor cells expressing either $bACE2_{R.cor}$ or hACE2. The bottom
1032 panels show the quantification of cell-cell fusion measuring the GFP+ area at 2, 6,
1033 12 hours (h) post-transfection. Data are presented as mean ± s.d., n = 2. The *P*
1034 values were determined by unpaired t-test. $*P < 0.05$, $**P < 0.01$, $***P < 0.001$;
1035 NS, not significant. **(I)** Different sarbecovirus S-proteins are sorted based on S-
1036 protein phylogenetics and grouped by RBD types defined structurally. Type-1
1037 strains are shown in red (SARS-CoV-2 clade) and blue (SARS-CoV-1 clade), type-
1038 2 strains in orange, type-3 strains in black and type-4 strains in green.
1039 Quantification of S-protein expression on the cell surface of effector cells by flow
1040 cytometry using an S2 antibody as the probe. Flow cytometry was repeated three
1041 times with representative data shown. **(J)** Effector cells shown in (**I**) were tested
1042 against receptor cells expressing hACE2 (gray line), $bACE2_{R.cor}$ (black line) and
1043 $bACE2_{R.cor}$-ΔGLC_{38} (green line, $bACE2_{R.cor}$ with the Thr40Ala mutation to remove
1044 the Asn38-glycan). Cell-cell fusion was quantified by assessing GFP+ areas (y-
1045 axis) at 4, 18, and 24 hours (h, x-axis) post-transfection (pt). Data are presented as
1046 mean ± s.d., n = 2. The *P* values were determined by unpaired t-test. $*P < 0.05$,
1047 $**P < 0.01$, $***P < 0.001$; NS, not significant. **(K)** Representative images of cell-
1048 cell fusion captured at 24 hours post-transfection are shown against receptor cells
1049 expressing different ACE2. Scale bar, 500 μm.

1050